Non-linear buckling analysis of thin-walled beams modeled with 7-parameter shell elements

Anh-Khoa Chau, Michael Brun, Pascal Ventura, Hamid Zahrouni, Michel Potier-Ferry

Non-linear buckling analysis of thin-walled beams modelled with 7-parameter shell elements

Anh-Khoa Chau[a], Michael Brun[a,*], Pascal Ventura[a], Hamid Zahrouni[a], Michel Potier-Ferry[a]

[a]*Université de Lorraine, Arts et Métiers Paris Tech, CNRS, LEM3, Metz F-57000, France*

Abstract

The non-linear quasi-static buckling of thin-walled beams with arbitrary cross-sections is studied by developing coupling strategies between the composing plates (web, flanges). The element adopted for modeling the plates is a 7-parameter shell element using the Enhanced Assumed Strain concept (Bütcher et al. (1994)). Different nodal shell directors exist at the interface between plates for thin-walled beams with arbitrary cross-sections, requiring appropriate strategies. The coupling between plates first considers Lagrange multipliers at the interface, following the mortar method on the surface between the plates. Second a simplified pre-processing method is proposed by modifying the shell directors of the nodes close to the interface. In the case of the quasi-static buckling of thin-walled beams with L-shaped and I-shaped cross-sections, the two coupling strategies are thoroughly assessed by using three different solution procedures: Newton-Raphson, Newton-Riks and Asymptotic Numerical Method (ANM). The pre-processing method is simple and turns out to be robust and efficient.

Keywords: Quasi-static non-linear buckling, Thin-walled structures, 7-parameter shell elements, Coupling mortar method, Shell directors, Asymptotic Numerical Method

1. Introduction

Thin-walled beams with arbitrary cross-sections, widely used in mechanical and civil engineering structures, are prone to experience local and global buckling phenomena. In Asgarian et al. (2013), Soltani et al. (2014), Soltani and Mohri (2016), the geometrically instabilities have been studied using finite element beam model and Asymptotic Numerical Method procedure (ANM). The ANM procedure is based on the decomposition of the displacement and path parameter as high order Taylor series and turned out to be a very competitive algorithm, able to efficiently predict the equilibrium path (Azrar et al. (1993), Cochelin et al. (1994a,b), Cochelin (1994), Cochelin et al. (2007)). The main advantages in comparison to Riks algorithm rely on the exponential convergence, the possibility to directly chain each loading ANM step from the previous one, without the need of correction stages as required by classical Newton-Riks algorithm. In addition, the ANM solving procedure only considers a constant tangent matrix for each order of the Taylor series and provides a natural continuation procedure by comparing the smallest term of the series with the biggest one. It leads to a posteriori adaptive step size for the ANM algorithm, providing a crucial advantage in comparison to classical Newton-Riks algorithm based on a priori step size. Numerous non-linear buckling analyses in the literature have shown

*Corresponding author : M. Brun, Université de Lorraine, Arts et Métiers Paris Tech, CNRS, LEM3, Metz F-57000, France

Email addresses: anh-khoa.chau@univ-lorraine.fr (Anh-Khoa Chau), michael.brun@univ-lorraine.fr (Michael Brun), pascal.ventura@univ-lorraine.fr (Pascal Ventura), hamid.zahrouni@univ-lorraine.fr (Hamid Zahrouni), michel.potier-ferry@univ-lorraine.fr (Michel Potier-Ferry)

that the number of loading steps is reduced as well as the computation time (Zahrouni et al. (1999), Najah et al. (1998), Jamal et al. (2002), Baguet and Cochelin (2003), Boutyour et al. (2004, 2006), Ventura et al. (2020, 2023)).

The ANM procedure has been extensively adopted for the analysis of the non-linear buckling of shell structures using the efficient 7-parameter shell element proposed by Bütcher et al. (1994), developed in the total Lagrangian framework. It is considered as a 'step into the third dimension' by adding an extra strain to the 6-parameter shell formulation, which takes into account the three mid-plane displacements, two rotations and the thickness stretch (Ramm and Wall (2004)). Indeed, the discrepancy between stress and strain variations across the shell thickness was dealt by adding an extra unknown, following the so-called Enhanced Assumed Strain (EAS) concept (Simo and Rifai (1990)). The main interest is to employ any linear and non-linear three-dimensional material laws without ad-hoc condensation technique, to deal with large strains without Poisson thickness locking phenomena (Bischoff and Ramm (1997, 2000)). It is shown that 7-parameter shell element is successful in reproducing buckling phenomena when the thickness of the shell structure goes to zero, meaning that the 7-parameter element is asymptotically correct, contrarily to the 6-parameter shell which displays strong deviation in comparison to the reference full three-dimensional continuum solution (Roehl and Ramm (1996)).
For the 7-parameter shell element, each node belonging to the mid-plane surface is associated with a nodal shell director. Nodal shell directors are easily obtained for plate and conical shape structures for which the shell director is known at every point of the mid-plane of the shell. It is not anymore the case for thin-walled beams with arbitrary cross-sections. In this situation, the plates, modeled with 7-parameter shell elements, have to be coupled together by adopting appropriate strategies. Rotation-free Kirchhoff-Love thin-shells, modeled using Isogeometric patches for the different plates composing the beams, are coupled by Herrema et al. (2019), Proserpio et al. (2021), using a penalty formulation to prescribe the displacement continuity and rotational continuity. The main drawback of the penalty method is to be problem-dependent because the penalty parameters should be carefully selected as high enough to ensure the continuity while avoiding excessive ill-conditioning. Mortar methods, requiring to solve a saddle point problem for the Lagrange multipliers, have also been proposed for the purpose of patch coupling (Dornisch et al. (2015), Brivadis et al. (2015)).

With the aim of simulating non-linear buckling problems of thin-walled beams with arbitrary cross-sections, the paper explores two strategies to take into account interfaces between plates. The first one is the mortar method, requiring the introduction of Lagrange multipliers computed on the surface defined at the interface between the plates. The method is very general and can be applied to conforming and non-conforming meshes at the interface. Nonetheless, a simplified method is also proposed, without introducing Lagrange multipliers, in order to keep the size of the original discretized problem. It is based on a simple pre-processing procedure in which the shell directors at the corner and middle

nodes of the adjacent 7-parameter shell elements, are determined as a function of the shell directors of the plates involved into the interface. The two coupling approaches are set up to study the non-linear quasi-static buckling phenomena of thin-walled beam structures with arbitrary cross-sections, using different solution strategies in order to thoroughly assess their efficiency and accuracy. It includes the classical Newton-Raphson, Newton-Riks and ANM strategies developed in the same MATLAB environment (MATLAB (2022)) for a fair comparison.

The paper is organized as follows. The shell kinematics along with EAS concept are briefly reminded in Section 2 before presenting the proposed coupling approaches, including the mortar method and the pre-processing method for dealing with arbitrary cross-sections of thin-walled beams. Solution procedures are briefly described in Section 3: two algorithms for Newton-Raphson with EAS are presented, as well as Riks algorithm and ANM procedure. In Section 4, two classical benchmarks for shell structures are first considered: the buckling of thin-walled beams with rectangular cross-section and the buckling of cylindrical shells. Then, the buckling behavior of L-shaped and I-shaped thin-walled beams is studied using the three solution strategies. Shell results are compared to reference results provided by three-dimensional computations with 20-node hexahedral elements. The accuracy and efficiency of both coupling approaches are evaluated in terms of mesh sensitivity for the different solution strategies. The pre-processing procedure with adjustment of shell directors at the interface between the web and flanges of the thin-walled beams turns out to be easy to set up, robust and accurate for reproducing the global and local non-linear buckling phenomena experienced by thin-walled beams.

2. Connection between 7-parameter shell elements with arbitrary angle at the interface for thin-walled beams

2.1. Shell kinematics of the 7-parameter shell element

The formulation of the 7-parameter shell element proposed by Bütcher et al. (1994) is widely adopted for buckling studies with large strains and rotations (Ramm and Wall (2004), Baguet and Cochelin (2003), Zahrouni et al. (1999)). In comparison to the classical 5-parameter shell, based on the Mindlin-Reissner kinematics assumption allowing for transverse shear deformations, the thickness change has been added as well as the Enhanced Assumed Strain (EAS), leading to the 7-parameter shell element. The key points of the 7-parameter shell element are reminded in the following.

The eight noded finite shell element is based on the Mindlin-Reissner kinematics assumption expressed in convective curvilinear coordinates. The shell kinematics is illustrated in Figure 1: A material point in the initial configuration $\mathbf{x}$ and in the deformed configuration $\bar{\mathbf{x}}$ can be described by assuming a linear variation of the displacement in the thickness direction as follows:

$$\begin{aligned} \mathbf{x}\left(\theta^1,\theta^2\right) &= \mathbf{r}\left(\theta^1,\theta^2\right) + \theta^3 \mathbf{a}_3\left(\theta^1,\theta^2\right) \\ \bar{\mathbf{x}}\left(\theta^1,\theta^2\right) &= \bar{\mathbf{r}}\left(\theta^1,\theta^2\right) + \theta^3 \bar{\mathbf{a}}_3\left(\theta^1,\theta^2\right) \end{aligned} \tag{1}$$

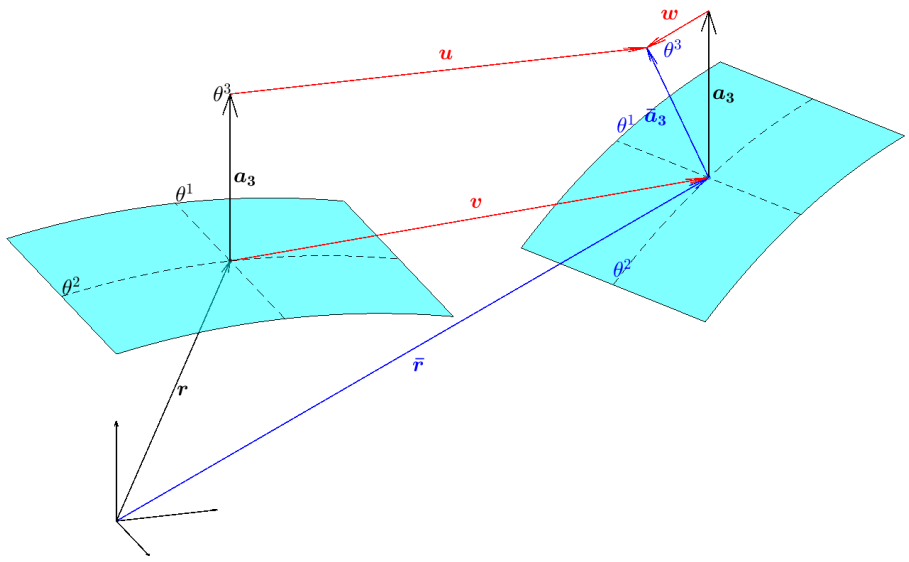

Figure 1: Shell geometry and kinematics

where $\mathbf{r}$ and $\bar{\mathbf{r}}$ are the projections of the material point in the initial and deformed configurations on the shell mid-surface, $\mathbf{a}_3$ and $\bar{\mathbf{a}}_3$ denote the shell directors at the projected point and $\left(\theta^1, \theta^2, \theta^3\right)$ are the convective curvilinear coordinates (with $\theta^i \in [-1, 1]\ \forall i \in [1, 2, 3]$). The displacement field is then defined as the difference between a material point in the deformed and undeformed configuration:

$$\mathbf{u} = \bar{\mathbf{x}} - \mathbf{x} = \mathbf{v}\left(\theta^1, \theta^2\right) + \theta^3 \mathbf{w}\left(\theta^1, \theta^2\right) \tag{2}$$

where $\mathbf{v}$ is the displacement at the mid-plane surface and $\mathbf{w}$ is the difference vector of the shell directors between the undeformed and deformed configurations.

For the description of the shell geometry and deformation, the covariant and contravariant bases vectors $\mathbf{g}_i$ and $\mathbf{g}^i$ are introduced:

$$\begin{aligned} &\mathbf{g}_i = \frac{\partial \mathbf{x}}{\partial \theta^i} = \mathbf{r}_{,i} + \theta^3 \mathbf{a}_{3,i} = \mathbf{a}_i + \theta^3 \mathbf{a}_{3,i} \quad \forall i \in [1, 2], \quad \mathbf{g}_3 = \frac{\partial \mathbf{x}}{\partial \theta^3} = \mathbf{a}_3 \\ &\mathbf{g}^i = \frac{\partial \theta^i}{\partial \mathbf{x}}, \quad \mathbf{g}^i \cdot \mathbf{g}_j = \delta^i_j \quad \forall i, j \in [1, 2, 3] \end{aligned} \tag{3}$$

With the base vectors in Eqs.(3), the material deformation gradient is given by:

$$\mathbf{F} = \frac{\partial \bar{\mathbf{x}}}{\partial \mathbf{x}} = \frac{\partial \bar{\mathbf{x}}}{\partial \theta} \cdot \frac{\partial \theta}{\partial \mathbf{x}} = \bar{\mathbf{g}}_i \otimes \mathbf{g}^i \tag{4}$$

From the displacement assumption, the Green Lagrange strain tensor is derived as:

$$\mathbf{E} = \frac{1}{2}\left[\mathbf{F}^T \mathbf{F} - \mathbf{I}\right] = \frac{1}{2}\left[\bar{\mathbf{g}}_i \cdot \bar{\mathbf{g}}_j - \mathbf{g}_i \cdot \mathbf{g}_j\right] \mathbf{g}^i \otimes \mathbf{g}^j = E_{ij}\, \mathbf{g}^i \otimes \mathbf{g}^j \tag{5}$$

Using Eqs.(3), the Green Lagrange strain tensor can be written in a form that contains constant, linear,

and quadratic terms in the thickness coordinate θ^3, denoted by α, β and γ, as follows:

$$\begin{aligned}\mathbf{E} &= \frac{1}{2}\left[\bar{\mathbf{a}}_i \cdot \bar{\mathbf{a}}_j - \mathbf{a}_i \cdot \mathbf{a}_j\right]\mathbf{g}^i \otimes \mathbf{g}^j + \frac{1}{2}\left[\bar{\mathbf{a}}_i \cdot \bar{\mathbf{a}}_{3,j} + \bar{\mathbf{a}}_j \cdot \bar{\mathbf{a}}_{3,i} - \mathbf{a}_i \cdot \mathbf{a}_{3,j} - \mathbf{a}_j \cdot \mathbf{a}_{3,i}\right]\theta^3\mathbf{g}^i \otimes \mathbf{g}^j \ldots \\ &\ldots + \frac{1}{2}\left[\bar{\mathbf{a}}_{3,i} \cdot \bar{\mathbf{a}}_{3,j} - \mathbf{a}_{3,i} \cdot \mathbf{a}_{3,j}\right]\left(\theta^3\right)^2\mathbf{g}^i \otimes \mathbf{g}^j = \left[\alpha_{ij} + \beta_{ij}\theta^3 + \gamma_{ij}\left(\theta^3\right)^2\right]\mathbf{g}^i \otimes \mathbf{g}^j \\ &= E_{ij}\,\mathbf{g}^i \otimes \mathbf{g}^j \quad \text{with } \mathbf{a}_{3,3} = \bar{\mathbf{a}}_{3,3} = 0 \quad \text{and} \quad \beta_{33} = 0\end{aligned} \tag{6}$$

The Green-Lagrange strain tensor can also be written in terms of displacement in the contravariant base of the initial configuration as follows (Bischoff and Ramm (2000)):

$$\mathbf{E} = \frac{1}{2}\left(\frac{\partial \mathbf{u}}{\partial \theta^i} \cdot \mathbf{g}_j + \frac{\partial \mathbf{u}}{\partial \theta^j} \cdot \mathbf{g}_i + \frac{\partial \mathbf{u}}{\partial \theta^i} \cdot \frac{\partial \mathbf{u}}{\partial \theta^j}\right)\mathbf{g}^i \otimes \mathbf{g}^j = \left[E^l_{ij}(\mathbf{u}) + E^{nl}_{ij}(\mathbf{u},\mathbf{u})\right]\mathbf{g}^i \otimes \mathbf{g}^j \tag{7}$$

where $\mathbf{E}^l(\mathbf{u})$ and $\mathbf{E}^{nl}(\mathbf{u},\mathbf{u})$ denote the linear and non-linear parts of the strain tensor $\mathbf{E}$.

Bütcher et al. (1994) showed that, if β_{33} is set to zero, a relative error will occur for the problems dominated mainly by bending. This undesired stiffening effect is called Poisson thickness locking and does nos vanish with the mesh refinement (Bischoff and Ramm (1997)). To alleviate this issue, Bütcher et al. (1994) proposed to improve the previous shell kinematics with an extra parameter, corresponding to an additional strain variable across the shell thickness. Thus the starting point of the enhanced assumed strain (EAS) is the introduction of a linearly varying strain in the thickness direction:

$$\begin{aligned}&E^*_{33} = \alpha_{33} + \theta^3\tilde{\beta}_{33} \\ &\mathbf{E}^*(\mathbf{u},\tilde{\mathbf{E}}) = \mathbf{E}(\mathbf{u}) + \tilde{\mathbf{E}} = \mathbf{E}^l(\mathbf{u}) + \mathbf{E}^{nl}(\mathbf{u},\mathbf{u}) + \tilde{\mathbf{E}} \\ &\tilde{\mathbf{E}} = \theta^3\tilde{\beta}_{33}\mathbf{g}^3 \otimes \mathbf{g}^3 \quad \text{with} \quad \tilde{\beta}_{33} = \tilde{\beta}_{33}(\theta_1,\theta_2)\end{aligned} \tag{8}$$

Herein, $\tilde{\mathbf{E}}$ denotes the EAS incompatible field and $\mathbf{E}^*(\mathbf{u},\tilde{\mathbf{E}})$ denotes the strain field with EAS field. By construction, the chosen $\tilde{\mathbf{E}}$ satisfies the orthogonality condition:

$$\int_\Omega \mathbf{S}(\mathbf{u},\tilde{\mathbf{E}})^T : \tilde{\mathbf{E}}\,d\Omega = 0 \tag{9}$$

The 2nd Piola-Kirchhoff stress tensor, denoted by $\mathbf{S}(\mathbf{u},\tilde{\mathbf{E}})$, is derived as:

$$\mathbf{S}(\mathbf{u},\tilde{\mathbf{E}}) = \mathbf{D} : \mathbf{E}^*(\mathbf{u},\tilde{\mathbf{E}}) = \mathbf{D} : \left(\mathbf{E}^l(\mathbf{u}) + \mathbf{E}^{nl}(\mathbf{u},\mathbf{u}) + \tilde{\mathbf{E}}\right) \tag{10}$$

where $\mathbf{D}$ is constitutive tensor. The strain energy is then written as:

$$W_{int}(\mathbf{u},\tilde{\mathbf{E}}) = \int_\Omega \frac{1}{2}\left[\mathbf{E}(\mathbf{u}) + \tilde{\mathbf{E}}\right)\Big]^T : \mathbf{S}(\mathbf{u},\tilde{\mathbf{E}})d\Omega \tag{11}$$

2.2. Finite Element discretization

Along the lines of Bütcher et al. (1994), the space approximation of the displacement and the geometry is given below:

$$\begin{aligned}\mathbf{x} &= \sum_{k=1}^{n} N^k\mathbf{r}^k + \theta^3 N^k\mathbf{a}_3^k \\ \mathbf{u} &= \sum_{k=1}^{n} N^k\mathbf{v}^k + \theta^3 N^k\mathbf{w}_3^k\end{aligned} \tag{12}$$

where the shape function depending on (θ^1, θ^2) is denoted by N^k, the nodal values by superscript k, and the number of nodes of the element by $n = 8$. Here, it is pointed out that the shell directors $\mathbf{a}_3^k$ is considered at each node k of the finite element mesh. In the case of two adjacent finite elements with an arbitrary angle at their interface, two different shell directors exist at the common nodes. For instance in the case of thin-walled beams with I-shaped cross-section, the common nodes between the flange and the web belong to three finite elements and different shell vectors can be defined at the interface. After presenting the finite element discretization of the 7-parameter shell element proposed by Bütcher et al. (1994), we focus on the strategies for dealing with arbitrary cross-section of thin-walled beams. By gathering the nodal displacements of the mid-plane surface, denoted by $\mathbf{v}$, and the difference vector between the shell directors, denoted by $\mathbf{w}$, into the kinematic vector denoted by $\mathbf{q}$, the space discretisation of the displacement field $\mathbf{u}$ and its variation $\delta\mathbf{u}$ are given by:

$$\mathbf{u} = [\mathbf{N}]\mathbf{q}, \quad \delta\mathbf{u} = [\mathbf{N}]\delta\mathbf{q} \tag{13}$$

where $[\mathbf{N}]$ is the shape function matrix given in Appendix A. Then, the linear and non-linear parts of the Green-Lagrange strain in Eq.(7) can be defined as:

$$\hat{\mathbf{E}}^{\mathrm{l}} = [\mathbf{R}][\mathbf{G}]\mathbf{q} = [\mathbf{B}^{\mathrm{l}}]\mathbf{q}, \qquad \hat{\mathbf{E}}^{\mathrm{nl}} = \frac{1}{2}[\mathbf{A}(\mathbf{q})][\mathbf{G}]\mathbf{q} = \frac{1}{2}[\mathbf{B}^{\mathrm{nl}}(\mathbf{q})]\mathbf{q} \tag{14}$$

where $\hat{\mathbf{E}}$ denotes the Voigt notation of the Green-Lagrange strain tensor, $[\mathbf{R}]$, $[\mathbf{G}]$ and $[\mathbf{A}(\mathbf{q})]$ are, respectively, the matrix composing the covariant base, the matrix of the gradients of the shape functions and the matrix of the displacement gradients, whose expressions are given in Appendix A. The variation of the linear part and the non-linear part of the strain tensors are expressed as follows:

$$\begin{aligned}
&\delta\hat{\mathbf{E}}^{\mathrm{l}} = [\mathbf{B}^{\mathrm{l}}]\delta\mathbf{q} \\
&\delta\hat{\mathbf{E}}^{\mathrm{nl}} = \frac{1}{2}[\mathbf{A}(\delta\mathbf{q})][\mathbf{G}]\mathbf{q} + \frac{1}{2}[\mathbf{A}(\mathbf{q})][\mathbf{G}]\delta\mathbf{q} = [\mathbf{A}(\mathbf{q})][\mathbf{G}]\delta\mathbf{q} = [\mathbf{B}^{\mathrm{nl}}(\mathbf{q})]\delta\mathbf{q} \\
&\delta\hat{\mathbf{E}} = \left([\mathbf{B}^{\mathrm{l}}] + [\mathbf{B}^{\mathrm{nl}}(\mathbf{q})]\right)\delta\mathbf{q} = [\bar{\mathbf{B}}(\mathbf{q})]\delta\mathbf{q}
\end{aligned} \tag{15}$$

Concerning the EAS field, the additional component $\tilde{\beta}_{33}$ does not require the continuity between adjacent finite elements. Thus, a simple bilinear space discretisation is assumed (Bütcher et al. (1994)):

$$\tilde{\beta}_{33} = \alpha_1 + \alpha_2\xi + \alpha_3\eta + \alpha_4\eta\xi \tag{16}$$

where ξ and η are the standard element coordinates. The additional unknown parameters α_1, α_2, α_3 and α_4 related to the EAS can be eliminated on the element level, thus the size of the original set of equations, related to the unknowns $\mathbf{q}$, is kept unchanged. The EAS strain tensor is then written in the matrix form as follows:

$$\hat{\tilde{\mathbf{E}}} = [\mathbf{B}_\alpha]\alpha \tag{17}$$

where expression of $[\mathbf{B}_\alpha]$ is given in Appendix A. As a result, the 2nd Piola-Kirchhoff stress tensor is given by:

$$\hat{\mathbf{S}} = [\mathbf{D}]\left([\mathbf{B}^{\mathrm{l}}]\mathbf{q} + \frac{1}{2}[\mathbf{B}^{\mathrm{nl}}(\mathbf{q})]\mathbf{q} + [\mathbf{B}_\alpha]\alpha\right) \tag{18}$$

where $[\mathbf{D}]$ is the matrix of elasticity.

2.3. Connection between two 7-parameter shell meshes

The problem of connecting two 7-parameter shell meshes arises when there is a discontinuity in the curvature at the interface of two meshes. Indeed, at the interface between the two meshes, the shell director is not unique anymore and it requires a numerical strategy for the coupling. The coupling problem is illustrated in Figure 2, representing two beams with L-shaped and T-shaped cross-sections. Contrarily to the case where the shell director can be determined without any ambiguity, such as for cylinders and spheres, here two shell directors exist at the edge between the adjacent plates. One way to avoid ambiguity is to consider cylindrical transition shell elements to link the two plates as proposed in (Baguet (2011)): The author added two cylindrical fitting shell elements to ensure the continuity of the shell director of the L-beam, so as a unique shell director can be defined at each node. Nonetheless, this method, requiring the addition of transition shell elements, does not respect the geometry and cannot be applied to more general cross-section profile such as a T-shaped cross-section. It is one of our main objective to use 7-parameter shell elements for arbitrary cross-sections of thin-walled beams. Thus, in the following, we propose two ways for coupling plates. The first one is based on the introduction of Lagrange multipliers according to the lines of the mortar approach (Bernardi et al. (1990, 1994), Brun et al. (2021), Chau et al. (2023)). The second strategy is a simplified strategy in which a unique shell director is assigned to each node close to the interface.

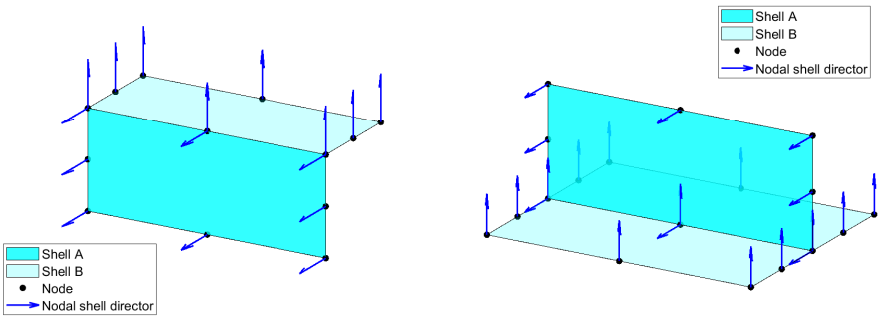

Figure 2: Discontinuity of the nodal shell directors for L-shaped and T-shaped cross-section thin-walled beams

2.3.1. Mortar approach

The mortar approach is based on a dual approach enabling us to take into account any kinematic relationships between the degrees of freedom by adding an interface virtual work in the principle of virtual works. Let us start by writing the governing equations without the interface contribution. In the case of conservative loads, the total energy of the system Π, also called the functional of the problem,

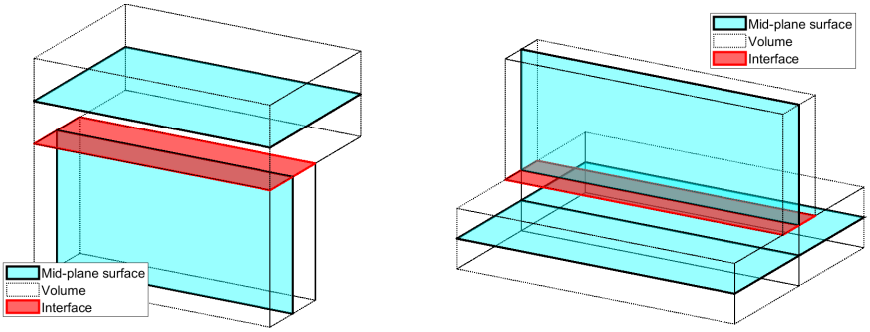

Figure 3: Mortar coupling surfaces (in red) for L-shaped and T-shaped cross-section thin-walled beams

is written as:

$$\begin{aligned} &\Pi(\mathbf{u},\tilde{\mathbf{E}}) = W_{\text{int}}(\mathbf{u},\tilde{\mathbf{E}}) - W_{\text{ext}}(\mathbf{u}) = W_{\text{int}}(\mathbf{u},\tilde{\mathbf{E}}) - \lambda P_e(\mathbf{u}) \\ &\text{with: } P_e(\mathbf{u}) = \int_\Omega \rho\mathbf{b}\cdot\mathbf{u}d\Omega + \int_\Gamma \mathbf{t}\cdot\mathbf{u}d\Gamma \end{aligned} \tag{19}$$

where $\rho\mathbf{b}$ are the body force and $\mathbf{t}$ the surface force acting on Γ. W_{int} is the strain energy given in Eq.(11). The applied body and surface forces are assumed to be proportional to a scalar loading parameter λ.

From the above equation, the variational form of the functional in Eq.(19) permits us to write the principle of virtual work as follows:

$$\begin{aligned} &\delta W_{\text{int}}(\mathbf{u},\tilde{\mathbf{E}}) = \delta W_{\text{ext}} \\ &\text{with: } \delta W_{\text{int}}(\mathbf{u},\tilde{\mathbf{E}}) = \int_\Omega \delta\mathbf{E}(\mathbf{u})^T : \mathbf{D} : \left[\mathbf{E}(\mathbf{u}) + \tilde{\mathbf{E}}\right] d\Omega \\ &\text{and } \delta W_{\text{ext}} = \lambda P_e(\delta\mathbf{u}) \end{aligned} \tag{20}$$

The above equation is completed with the variational form of the orthogonality condition:

$$\int_\Omega \mathbf{S}(\mathbf{u},\tilde{\mathbf{E}})^T : \delta\tilde{\mathbf{E}} = 0 \tag{21}$$

Eqs.(10),(20), and (21) are the governing equations of the quasi-static geometrically non-linear problem.

In the case of the connection between plates, we denote the plate A as the slave part and the plate B as the master part, connected between each other with the interface denoted S, as illustrated in Figure 3 in the cases of the L-shaped and T-shaped cross-sections. It can be seen that the coupling interface corresponds to a rectangular surface whose transverse size is equal to the thickness of the slave plate A. The coupling strategy is based on the introduction of an interface virtual work in the principle of virtual work as follows:

$$\begin{aligned} &\delta W_{\text{int}}(\mathbf{u},\tilde{\mathbf{E}}) = \delta W_{\text{ext}} + \delta W_{\text{interface}}(\lambda) \\ &\text{with: } \delta W_{\text{interface}}(\lambda) = \int_S \lambda(\delta\mathbf{u}_A - \delta\mathbf{u}_B)dS \end{aligned} \tag{22}$$

with λ corresponding to the Lagrange multiplier field on the coupling surface S. The virtual displacements associated with plates A and B are approximated in space on the surface S as:

$$\begin{aligned} \delta \mathbf{u}_{\mathrm{A}} &= [\mathbf{N_A}]\delta \mathbf{q}_{\mathrm{A}} \\ \delta \mathbf{u}_{\mathrm{B}} &= [\mathbf{N_B}]\delta \mathbf{q}_{\mathrm{B}} \end{aligned} \tag{23}$$

where the displacement variations $\delta \mathbf{q}_{\mathrm{A}}$ and $\delta \mathbf{q}_{\mathrm{B}}$ relate to the nodes of the slave and master side, respectively. According to the standard mortar method, the Lagrange multiplier field is approximated with the same shape functions as the displacements related to the slave side (plate A):

$$\lambda = [\mathbf{N_A}]\Lambda \tag{24}$$

where Λ gathers the Lagrange multipliers related to the nodes of the slave side. Taking into account the space discretisation of both displacements and Lagrange multipliers, the interface virtual work can be discretized in space as:

$$\delta W_{\mathrm{interface}}(\lambda) = \delta \mathbf{q}_{\mathrm{A}}^{\mathrm{T}}[\mathbf{L_A}]^{\mathrm{T}}\Lambda + \delta \mathbf{q}_{\mathrm{B}}^{\mathrm{T}}[\mathbf{L_B}]^{\mathrm{T}}\Lambda \tag{25}$$

where $[\mathbf{L_A}]$ and $[\mathbf{L_B}]$ are the mortar matrices, obtained by integrating the products of shape functions on the coupling surface S as:

$$\begin{aligned} [\mathbf{L}_{\mathrm{A}}] &= \int_{\mathrm{S}} [\mathbf{N_A}]^{\mathrm{T}}[\mathbf{N_A}]\mathrm{dS} \\ [\mathbf{L}_{\mathrm{B}}] &= \int_{\mathrm{S}} [\mathbf{N_A}]^{\mathrm{T}}[\mathbf{N_B}]\mathrm{dS} \end{aligned} \tag{26}$$

Using the two mortar operators, the kinematic relationship at the coupling surface S, corresponding to the displacement continuity, writes as:

$$[\mathbf{L}_{\mathrm{A}}]\mathbf{q}_{\mathrm{A}} + [\mathbf{L}_{\mathrm{B}}]\mathbf{q}_{\mathrm{B}} = 0 \tag{27}$$

2.3.2. Pre-processing procedure for the shell directors at the interface

The second approach proposed for coupling plates is based on the choice of a unique shell director at the nodes belonging to the common edge, depending on the shell directors of the two plates. The idea is illustrated in Figure 2 for L-shaped and T-shaped cross-section beams with two plates A and B of different thicknesses, with shell directors denoted by $\mathbf{a_3^A}$ and $\mathbf{a_3^B}$, respectively. At the corner node, the unique shell director is determined as the sum of the shell directors of the plates A and B as:

$$\mathbf{a_{3,corner}} = \mathbf{a_3^A} + \mathbf{a_3^B} \tag{28}$$

The shell directors are also modified at the middle nodes of the adjacent 8-node elements at both sides A and B of the corner as follows:

$$\begin{aligned} \mathbf{a^A_{3,middle}} &= \frac{1}{2}(\mathbf{a_{3,corner}} + \mathbf{a_3^A}) \\ \mathbf{a^B_{3,middle}} &= \frac{1}{2}(\mathbf{a_{3,corner}} + \mathbf{a_3^B}) \end{aligned} \tag{29}$$

In Figure 4, shell directors are plotted at the nodes belonging to the adjacent 8-node elements, on both sides of the corner node, as well as the shell director field derived from the quadratic shape functions. In the case of T-shaped cross-section, the same strategy can be applied as shown in Figure 4.

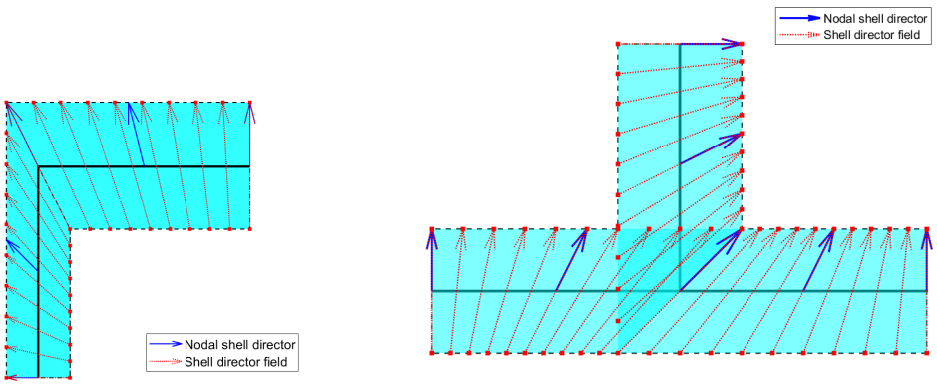

(a) L-shaped cross-section (b) T-profile cross-section

Figure 4: Spatial discretization of the shell directors $\mathbf{a_3}$ for two adjacent 8-node shell elements: (a) L-shaped cross-section; (b) T-profile cross-section

It has to be noted that this simplified strategy for connecting two 8-node 7-parameter shell meshes requires a simple pre-processing procedure in order to prescribe the shell directors at the corner and middle nodes of the adjacent finite elements. In comparison to the dual method previously proposed, a small deterioration of the obtained numerical results could be expected because the dual strategy only requires the introduction of the Lagrange multipliers without changing the shell directors of the adjacent elements. In addition, for both coupling strategies, smaller elements at the interface should be considered in comparison to the remaining of the mesh. The effect of the shell director assumption will be studied in detail in the numerical application for complex buckling problems of L-shaped and I-shaped cross-section thin-walled beams, by considering different meshes with or without smaller elements at the interface between the plates. Results using shell elements will be compared to reference results provided by a full 3D refined approach using hexahedral elements with quadratic shape functions. Finally, it is worth noting that the simplified approach does not require the introduction of additional quantities, which permits us to conserve the size of the original discretized problem.

3. Solving procedures for quasi-static geometrically non-linear problems modeled with 7-parameter shell elements

In order to thoroughly assess the previous coupling approaches for predicting quasi-static buckling of thin-walled beams, this section presents three different solution procedures: Newton-Raphson iterative procedure, Riks arc-length method and Asymptotic Numerical Method (ANM). First, the classical Newton-Raphson iterative procedure is reminded in the case of 7-parameter shell element (Bischoff

and Ramm (1997)) in order to derive an improved version of this classical procedure able to deal more efficiently with EAS field. Then Riks arc-length method is presented. Finally, ANM strategy is briefly presented by reporting the details in Appendix B. In comparison to Riks method, ANM is much more flexible because the size of the loading step automatically adjusts to the physics, that is the step only becomes very small at the neighboring of the bifurcation points. In the numerical application section, the reference results are provided by a fine mesh composed of 20-node hexahedral elements using ANM procedure. Algorithms are given for the three solution strategies and are implemented in the same environment (MATLAB (2022)) in order to compare their efficiency for predicting the equilibrium path and bifurcation points.

3.1. Newton-Raphson iterative procedure

From the finite element discretization presented in Section (2.2), the governing equations in Eqs. (10),(20) and (21) can be written as:

$$\begin{cases} \mathbf{R} = \mathbf{f}_{\text{int}}(\mathbf{q},\alpha) - \lambda\mathbf{P} = \bigwedge_{n=1}^{N_e}\left[\int_{\Omega_e}[\bar{\mathbf{B}}(\mathbf{q})]^T\hat{\mathbf{S}}\,d\Omega\right] - \lambda\mathbf{P} = 0 \\ \mathbf{R}^e_\alpha = \int_{\Omega_e}[\mathbf{B}_\alpha]^T\hat{\mathbf{S}}\,d\Omega = 0 \\ \hat{\mathbf{S}} = [\mathbf{D}]\left([\mathbf{B}^l] + \frac{1}{2}[\mathbf{B}^{nl}(\mathbf{q})]\mathbf{q} + [\mathbf{B}_\alpha]\alpha\right) \end{cases} \tag{30}$$

where $\mathbf{R}$ and $\mathbf{R}^e_\alpha$ denote, respectively, the global residual vector of the equilibrium equation of the system and the elementary residual vector of the orthogonality condition, $\hat{\mathbf{S}}$ is the second Piola-Kirchhoff stress tensor, $\bigwedge_{n=1}^{N_e}$ is the assembling operator, N_e is the number of finite elements, and $\mathbf{f}_{\text{ext}}$ is the global external force vector.

The system in Eq.(30) describes the non-linear problem with the nodal displacements of the mid-plane surface and the difference vectors of shell directors, gathered in $\mathbf{q}$, the additional EAS α quantities and the load parameter λ. The system can be solved by prescribing λ and using the iterative Newton-Raphson method which requires the linearization of the first two equations in the system. Considering that the solution at k^{th} iteration $\mathbf{q}^{(k)}$ and $\alpha^{(k)}$ are known, the solution at $(k+1)^{th}$ iteration can be found from:

$$\begin{aligned} &\mathbf{R}^{(k+1)} = \mathbf{R}^{(k)} + \frac{\partial\mathbf{f}_{\text{int}}}{\partial\mathbf{q}}\delta\mathbf{q} + \frac{\partial\mathbf{f}_{\text{int}}}{\partial\alpha}\delta\alpha = \mathbf{R}^{(k)} + \bigwedge_{n=1}^{N_e}\left([\mathbf{K}_{uu}]\delta\mathbf{q}^e + [\mathbf{K}_{\alpha u}]^T\delta\alpha^e\right) = 0 \\ &\mathbf{R}^{e(k+1)}_\alpha = \mathbf{R}^{e(k)}_\alpha + \frac{\partial\mathbf{R}^e_\alpha}{\partial\mathbf{q}}\delta\mathbf{q}^e + \frac{\partial\mathbf{R}^e_\alpha}{\partial\alpha}\delta\alpha^e = \mathbf{R}^{e(k)}_\alpha + [\mathbf{K}_{\alpha u}]\delta\mathbf{q}^e + [\mathbf{K}_{\alpha\alpha}]\delta\alpha^e = 0 \\ &\mathbf{q}^{(k+1)} = \mathbf{q}^{(k)} + \delta\mathbf{q}, \qquad \alpha^{e(k+1)} = \alpha^{e(k)} + \delta\alpha^e \end{aligned} \tag{31}$$

From the second equation in Eq.(31), the relation between $\delta\alpha^e$ and $\delta\mathbf{q}^e$ is given by:

$$\delta\alpha^e = -[\mathbf{K}_{\alpha\alpha}]^{-1}\left(\mathbf{R}^{e(k)}_\alpha + [\mathbf{K}_{\alpha u}]\delta\mathbf{q}^e\right) \tag{32}$$

Substituting the above relation into Eq.(31), we obtain:

$$[\mathbf{K}_T]\delta\mathbf{q} = -\mathbf{R}^{(k)} + \bigwedge_{n=1}^{N_e}\left([\mathbf{K}_{\alpha u}]^T[\mathbf{K}_{\alpha\alpha}]^{-1}\mathbf{R}^{e(k)}_\alpha\right) \tag{33}$$

where $[\mathbf{K}_T]$ is the tangent stiffness matrix whose expression is given below:

$$[\mathbf{K}_T] = \bigwedge_{n=1}^{N_e} \left([\mathbf{K}_{uu}] - [\mathbf{K}_{\alpha u}]^T [\mathbf{K}_{\alpha\alpha}]^{-1} [\mathbf{K}_{\alpha u}] \right) \tag{34}$$

The elementary matrices intervening in the tangent stiffness matrix are:

$$\begin{aligned}
[\mathbf{K}_{uu}] &= \int_{\Omega_e} [\bar{\mathbf{B}}(\mathbf{q}^{(k)})]^T [\mathbf{D}] [\bar{\mathbf{B}}(\mathbf{q}^{(k)})] \, d\Omega_e + \int_{\Omega_e} [\mathbf{G}]^T [\mathbf{M}] [\mathbf{G}] \, d\Omega_e \\
[\mathbf{K}_{\alpha u}] &= \int_{\Omega_e} [\mathbf{B}_\alpha]^T [\mathbf{D}] [\bar{\mathbf{B}}(\mathbf{q}^{(k)})] \, d\Omega_e \\
[\mathbf{K}_{\alpha\alpha}] &= \int_{\Omega_e} [\mathbf{B}_\alpha]^T [\mathbf{D}] [\mathbf{B}_\alpha] \, d\Omega_e
\end{aligned} \tag{35}$$

where the expressions of the above matrices can be found in Appendix A. The algorithm to find the solution $(\mathbf{q}_0 + \Delta\mathbf{q}, \alpha_0 + \Delta\alpha, \lambda_0 + \Delta\lambda)$ from $(\mathbf{q}_0, \alpha_0, \lambda_0)$ is summarized in Algorithm 1.

Algorithm 1 Newton-Raphson procedure with EAS

Require: $\mathbf{q}_0, \alpha_0, \lambda_0, \Delta\lambda$

Set $(\mathbf{q}^{(0)}, \alpha^{(0)}) = (\mathbf{q}_0, \alpha_0)$

Evaluate $[\mathbf{K}_T] = [\mathbf{K}_T(\mathbf{q}^{(0)})]$ and $\mathbf{f}_{int} = \mathbf{f}_{int}(\mathbf{q}^{(0)}, \alpha^{(0)})$

Evaluate residual vector $\mathbf{R}^{(0)} = \mathbf{R}(\mathbf{q}^{(0)}, \alpha^{(0)}, \lambda_0 + \Delta\lambda)$

Evaluate residual vector $\mathbf{R}_\alpha^{(0)} = \mathbf{R}_\alpha(\mathbf{q}^{(0)}, \alpha^{(0)})$ and the term $\bigwedge_{n=1}^{N_e} \left([\mathbf{K}_{\alpha u}]^T [\mathbf{K}_{\alpha\alpha}]^{-1} \mathbf{R}_\alpha^{e(k)} \right)$

Set $k = 0$

while $k \leq N_{max}$ **do** ▷ N_{max} is user-defined maximum iteration

Evaluate $\delta\mathbf{q}$ from Eq.(33) and $\mathbf{q}^{(k+1)} = \mathbf{q}^{(k)} + \delta\mathbf{q}$

Evaluate $\delta\alpha^e$ from Eq.(32) and $\alpha^{e(k+1)} = \alpha^{e(k)} + \delta\alpha^e$

Evaluate $[\mathbf{K}_T] = [\mathbf{K}_T(\mathbf{q}^{(k+1)})]$ and $\mathbf{f}_{int} = \mathbf{f}_{int}(\mathbf{q}^{(k+1)}, \alpha^{(k+1)})$

Evaluate global residual vector $\mathbf{R}^{(k+1)} = \mathbf{R}(\mathbf{q}^{(k+1)}, \alpha^{(k+1)}, \lambda_0 + \Delta\lambda)$

Evaluate local residual vectors $\mathbf{R}_\alpha^{(k+1)} = \mathbf{R}_\alpha(\mathbf{q}^{(k+1)}, \alpha^{(k+1)}$ and $\bigwedge_{n=1}^{N_e} \left([\mathbf{K}_{\alpha u}]^T [\mathbf{K}_{\alpha\alpha}]^{-1} \mathbf{R}_\alpha^{e(k+1)} \right)$

Evaluate $\varepsilon = \max\{\| \mathbf{R}^{(k+1)} \|, \| \mathbf{R}_\alpha^{(k+1)} \|\}$

if $\varepsilon \leq \varepsilon_{NR}$ **then** ▷ ε_{NR} is user-defined tolerance

$\Delta\mathbf{q} = \mathbf{q}^{(k+1)} - \mathbf{q}_0$ and $\Delta\alpha = \alpha^{(k+1)} - \alpha_0$

break

else

$k = k + 1$

end if

end while

3.2. Improved Newton-Raphson iterative procedure for EAS

Another procedure can be applied in which the increment $\delta\alpha^e$ is not needed. In order to do that, the relation between α^e and $\mathbf{q}^e$ is exactly ensured from the orthogonality condition in Eq.(30) as follows:

$$\alpha^{e(k+1)} = -[\mathbf{K}_{\alpha\alpha}]^{-1} \int_\Omega^e [\mathbf{B}_\alpha]^T [\mathbf{D}] \left([\mathbf{B}^l] + \frac{1}{2} [\mathbf{B}^{nl}(\mathbf{q}^{e(k+1)})] \right) \mathbf{q}^{e(k+1)} \, d\Omega \tag{36}$$

This relation permits us first to determine $\mathbf{f}_{\text{int}}$ from only the displacement $\mathbf{q}$ and secondly to prescribe directly the orthogonality condition in Eq.(30). Therefore, the linearization problem becomes:

$$
\begin{aligned}
&[\mathbf{K}_T]\delta\mathbf{q} = -\mathbf{R}^{(k)}, \qquad \mathbf{q}^{(k+1)} = \mathbf{q}^{(k)} + \delta\mathbf{q} \\
&\alpha^{e(k+1)} = -[\mathbf{K}_{\alpha\alpha}]^{-1} \int_{\Omega}^{e} [\mathbf{B}_\alpha]^T [\mathbf{D}] \left([\mathbf{B}^l] + \frac{1}{2}[\mathbf{B}^{nl}(\mathbf{q}^{e(k+1)})] \right) \mathbf{q}^{e(k+1)} \, d\Omega \\
&\mathbf{R}^{(k+1)}(\mathbf{q}^{(k+1)}, \alpha^{(k+1)}) = \mathbf{R}^{(k+1)}(\mathbf{q}^{(k+1)})
\end{aligned}
\tag{37}
$$

The above system allows solving the non-linear problem of the 7-parameter shell element by linearizing only the global residual vector of the equilibrium equation without linearizing the residual of the orthogonality condition.

The algorithm to find the solution $(\mathbf{q}_0 + \Delta\mathbf{q}, \lambda_0 + \Delta\lambda)$ from $(\mathbf{q}_0, \lambda_0)$ is given in Algorithm 2. It can be seen that Algorithm 2 is simplified in comparison to Algorithm 1. In addition, the main advantage is that we do not need anymore to save the EAS quantities at every integration point, for every Newton-Raphson iteration step, reducing the memory requirement during the computation. Finally, it will be shown in the following that the number of iterations is slightly decreased thanks to this improved Newton-Raphson algorithm for the 7-parameter shell elements.

Algorithm 2 Improved Newton-Raphson procedure with EAS

Require: $\mathbf{q}_0, \lambda_0, \Delta\lambda$

Set $(\mathbf{q}^{(0)}, \alpha^{(0)}) = (\mathbf{q}_0, \alpha_0)$

Evaluate $[\mathbf{K}_T] = [\mathbf{K}_T(\mathbf{q}^{(0)})]$ and $\mathbf{f}_{\text{int}} = \mathbf{f}_{\text{int}}(\mathbf{q}^{(0)}, \alpha^{(0)})$

Evaluate residual vector $\mathbf{R}^{(0)} = \mathbf{R}(\mathbf{q}^{(0)}, \alpha^{(0)}, \lambda_0 + \Delta\lambda)$

Set $k = 0$

while $k \leq N_{max}$ **do** ▷ N_{max} is user-defined maximum iteration

  Evaluate $\delta\mathbf{q} = -[\mathbf{K}_T]^{-1}\mathbf{R}^{(k)}$ and $\mathbf{q}^{(k+1)} = \mathbf{q}^{(k)} + \delta\mathbf{q}$

  Evaluate $\alpha^{e(k+1)}$ from Eq.(36)

  Evaluate $[\mathbf{K}_T] = [\mathbf{K}_T(\mathbf{q}^{(k+1)})]$ and $\mathbf{f}_{\text{int}} = \mathbf{f}_{\text{int}}(\mathbf{q}^{(k+1)}, \alpha^{(k+1)})$

  Evaluate residual vector $\varepsilon = \mathbf{R}^{(k+1)} = \mathbf{R}(\mathbf{q}^{(k+1)}, \alpha^{(k+1)}, \lambda_0 + \Delta\lambda)$

  if $\varepsilon \leq \varepsilon_{NR}$ **then** ▷ ε_{NR} is user-defined tolerance

    $\Delta\mathbf{q} = \mathbf{q}^{(k+1)} - \mathbf{q}_0$

    break

  else

    $k = k + 1$

  end if

end while

3.3. Riks arc-length method

The Newton-Raphson method presented in the previous section can be applied to solve any non-linear problem. However, a disadvantage of the Newton-Raphson method is that the equilibrium path

exhibiting more than one critical point cannot be completely found. In such cases, the snap-through and snap-back phenomena are observed while using the load-control or displacement-control Newton-Raphson procedure by prescribing an increasing value of the λ parameter. To overcome this problem, Riks proposed the arc-length method in which λ is considered as a variable of the problem by adding an arc-length condition to the original problem (ABAQUS (2014)). Thus, the problem becomes:

$$\begin{cases} \mathbf{R}(\mathbf{q},\alpha,\lambda) = \mathbf{f}_{\text{int}}(\mathbf{q},\alpha) - \lambda\mathbf{P} = \mathbf{f}_{\text{int}}(\mathbf{q}_0+\Delta\mathbf{q},\alpha_0+\Delta\alpha) - (\lambda_0+\Delta\lambda)\mathbf{P} = 0 \\ \mathbf{R}^e_\alpha = \displaystyle\int_\Omega [\mathbf{B}_\alpha]^T[\mathbf{D}]\left([\mathbf{B}^l] + \frac{1}{2}[\mathbf{B}^{nl}(\mathbf{q}^e)]\mathbf{q}^e + [\mathbf{B}_\alpha]\alpha^e\right) d\Omega = 0 \\ s^2 = \langle \mathbf{q}-\mathbf{q}_0, \mathbf{q}-\mathbf{q}_0\rangle + (\lambda-\lambda 0)^2 = \langle \Delta\mathbf{q},\Delta\mathbf{q}\rangle + \Delta\lambda^2 \end{cases} \tag{38}$$

where arc-length s is a user parameter, $\Delta\mathbf{q}$ and $\Delta\lambda$ are the increments from the initial solutions $(\mathbf{q}_0,\lambda_0)$ to the target solution $(\mathbf{q},\lambda)$. By directly taking into account the orthogonality condition as previously presented, we can linearize the system along the displacement and the arc-length parameter, without considering the linearization of the EAS parameter α as follows:

$$\begin{cases} R^{(k+1)} = R^{(k)} + [\mathbf{K}_T(\mathbf{q}^{(k)})]\delta\mathbf{q} - \delta\lambda\mathbf{P} \\ \alpha^{e(k+1)} = -[\mathbf{K}_{\alpha\alpha}]^{-1}\displaystyle\int_{\Omega^e}[\mathbf{B}_\alpha]^T[\mathbf{D}]\left([\mathbf{B}^l] + \frac{1}{2}[\mathbf{B}^{nl}(\mathbf{q}^{e(k+1)})]\right)\mathbf{q}^{e(k+1)}\, d\Omega \\ \langle \Delta\mathbf{q}^{(k)} + \delta\mathbf{q}, \Delta\mathbf{q}^{(k)} + \delta\mathbf{q}\rangle + (\Delta\lambda^{(k)} + \delta\lambda)^2 - s^2 = 0 \\ \Delta\mathbf{q}^{(k+1)} = \Delta\mathbf{q}^{(k)} + \delta\mathbf{q}, \qquad \text{and} \qquad \Delta\lambda^{(k+1)} = \Delta\lambda^{(k)} + \delta\lambda \end{cases} \tag{39}$$

Here, various techniques can be employed to solve the above system. We adopt below the technique described in ABAQUS (2014) in which the arc-length condition is imposed on the prediction part of the solution and the correction part is sought in the perpendicular direction of the prediction solution. The algorithm is given in Algorithm 3.

It can be observed that the prediction part $\delta\lambda = \dfrac{\pm s}{\sqrt{\langle \delta\mathbf{q}_\mathbf{F}, \delta\mathbf{q}_\mathbf{F}\rangle + 1}}$ gives two different solutions $\delta\lambda$: one solution leads to the desired forward progress on the equilibrium path while the other leads to a previous converged solution. Here, the criterion enabling us to choose the forward loading progress, is given below:

$$\delta\lambda\langle \delta\hat{\mathbf{q}}, \Delta\mathbf{u}_0\rangle + \delta\lambda\Delta\lambda_0 > 0 \tag{40}$$

where $\Delta\mathbf{q}_0$ and $\Delta\lambda_0$ are the increments of the previous converged solution.

3.4. Asymptotic-numerical Method

3.4.1. Perturbation technique

The governing equations of a quasi-static non-linear problem for a 7-parameter shell structure in Eqs. (8), (10), (20) and (21) can be rewritten in terms of displacement $\mathbf{u}$, second Piola-Kirchhoff stress

Algorithm 3 Newton-Riks procedure

Require: $\mathbf{q}_0, \lambda_0$ and arc-length s

Set $(\mathbf{q}^{(0)}, \alpha^{(0)}) = (\mathbf{q}_0, \alpha_0)$ and evaluate $[\mathbf{K}_T] = [\mathbf{K}_T(\mathbf{q}^{(0)})]$ and $\mathbf{f}_{int} = \mathbf{f}_{int}(\mathbf{q}^{(0)}, \alpha^{(0)})$

Set $k = 1$

while $k \leq N_{max}$ **do**

if $k = 1$ **then** ▷ Prediction part

Evaluate $\delta\mathbf{q_F} = [\mathbf{K}_T(\mathbf{q}_0)]^{-1}\mathbf{P}$, $\delta\lambda = \dfrac{\pm s}{\sqrt{\langle \delta\mathbf{q_F}, \delta\mathbf{q_F}\rangle + 1}}$ and $\delta\mathbf{q} = \delta\lambda\ \delta\mathbf{q_F}$

else ▷ Correction part

Evaluate $\delta\mathbf{q}_R = [\mathbf{K}_T(\mathbf{q}^{(k)}]^{-1}\mathbf{R}^{(k)}$ and $\delta\mathbf{q}_F = [\mathbf{K}_T(\mathbf{q}^{(k)})]^{-1}\mathbf{P}$

Evaluate $\delta\lambda = \dfrac{-\langle \delta\mathbf{q}_R, \Delta\mathbf{q}^{(1)}\rangle}{\langle \delta\mathbf{q}_F, \Delta\mathbf{q}^{(1)}\rangle + \Delta\lambda^{(1)}}$ and $\delta\mathbf{q} = \delta\mathbf{q}_R + \delta\lambda\ \delta\mathbf{q}_F$

end if

Evaluate $\mathbf{q}^{(k+1)} = \mathbf{q}^{(k)} + \delta\mathbf{q}^{(k+1)}$ and $\lambda^{(k+1)} = \lambda^{(k)} + \delta\lambda^{(k+1)}$

Evaluate $\alpha^{e(k+1)}$ from Eq.(36)

Evaluate $[\mathbf{K}_T] = [\mathbf{K}_T(\mathbf{q}^{(k+1)})]$ and $\mathbf{f}_{int} = \mathbf{f}_{int}(\mathbf{q}^{(k+1)}, \alpha^{(k+1)})$

Evaluate residual vector $\varepsilon = \mathbf{R}^{(k+1)} = \mathbf{R}(\mathbf{q}^{(k+1)}, \alpha^{(k+1)}, \lambda^{(k+1)})$

if $\varepsilon \leq \varepsilon_{NR}$ **then**

$\Delta\mathbf{q} = \mathbf{q}^{(k+1)} - \mathbf{q}_0$ and $\Delta\lambda = \lambda^{(k+1)} - \lambda_0$

break

else

$k = k + 1$

end if

end while

$\mathbf{S}$ and additional enhanced strain $\tilde{\mathbf{E}}$ as follows:

$$\begin{cases} \int_\Omega [\mathbf{E}^{\mathrm{l}}(\delta\mathbf{u}) + 2\mathbf{E}^{\mathrm{nl}}(\mathbf{u},\delta\mathbf{u})]^{\mathsf{T}} : \mathbf{S}\, \mathrm{d}\Omega = \lambda P_e(\delta\mathbf{u}) \\ \mathbf{S}(\mathbf{u},\tilde{\mathbf{E}}) = \mathbf{D} : \left(\mathbf{E}^{\mathrm{l}}(\mathbf{u}) + \mathbf{E}^{\mathrm{nl}}(\mathbf{u},\mathbf{u}) + \tilde{\mathbf{E}}\right) \\ \int_\Omega \delta\tilde{\mathbf{E}}^{\mathsf{T}} : \mathbf{S}(\mathbf{u},\tilde{\mathbf{E}})\, \mathrm{d}\Omega = 0 \end{cases} \tag{41}$$

The system in Eq.(41) includes the equilibrium, the constitutive equation, and the orthogonality condition for the additional strain. In order to apply the perturbation technique, a mixed variable $\mathbf{V}$ is introduced as below:

$$\mathbf{V} = \begin{pmatrix} \mathbf{u} \\ \mathbf{S} \\ \tilde{\mathbf{E}} \end{pmatrix} \tag{42}$$

Using the mixed vector above, the system in Eq.(41) can be rewritten as:

$$\mathbf{L}(\mathbf{V}) + \mathbf{Q}(\mathbf{V},\mathbf{V}) = \lambda\mathbf{F} \tag{43}$$

where $\mathbf{L}(.)$ and $\mathbf{Q}(.,.)$ are respectively the linear and quadratic operators, and $\mathbf{F}$ is a known vector. Their expressions are given in Appendix B.

Assuming there exists an initial solution $(\mathbf{V}_0,\lambda_0)$ to Eq.(43), the solution $(\mathbf{V},\lambda)$ can be expanded, in the neighborhood of the initial solution, in terms of a path parameter "a" as follows:

$$\begin{aligned} \mathbf{V}(a) &= \mathbf{V}_0 + \sum_{p=1}^{\infty} a^p \mathbf{V}_p = \mathbf{V}_0 + a\mathbf{V}_1 + a^2\mathbf{V}_2 + ... \\ \lambda(a) &= \lambda_0 + \sum_{p=1}^{\infty} a^p \lambda_p = \lambda_0 + a\lambda_1 + a^2\lambda_2 + ... \\ a &= \langle \mathbf{u} - \mathbf{u}_0, \mathbf{u}_1 \rangle + (\lambda - \lambda_0)\lambda_1 \end{aligned} \tag{44}$$

where we have defined the mixed variable at order "p", denoted by $\mathbf{V}_p$ by $(\mathbf{u}_p, \mathbf{S}_p, \tilde{\mathbf{E}}_p)^{\mathsf{T}}$, gathering the displacement, the second Piola-Kirchhoff stress and the additional strain at order "p". A good choice for the path parameter "a" is the linearized arc-length parameter which corresponds to the projection of the increment of the solution in the tangent direction $\mathbf{u}_1, \lambda_1$. Substituting the above expansion to Eq.(43), we obtain:

$$\begin{aligned} &\sum_{p=1}^{\infty} a^p \mathbf{L}(\mathbf{V}_p) + 2\sum_{p=1}^{\infty} a^p \mathbf{Q}(\mathbf{V}_0,\mathbf{V}_p) + \mathbf{Q}\Big(\sum_{p=1}^{\infty} a^p\mathbf{V}_p, \sum_{p=1}^{\infty} a^p\mathbf{V}_p\Big) = \sum_{p=1}^{\infty} a^p\lambda_p\mathbf{F} \\ &\text{and } a = \sum_{p=1}^{\infty} \langle \mathbf{u}_p, \mathbf{u}_1 \rangle + \sum_{p=1}^{\infty} \lambda_p\lambda_1 \end{aligned} \tag{45}$$

Equating the above system in terms of the power of "a", the following sequence of linear problems is obtained:

Order $p = 1$:

$$\mathbf{L}(\mathbf{V}_1) + 2\mathbf{Q}(\mathbf{V}_0,\mathbf{V}_1) = \lambda_1\mathbf{F} \qquad\qquad \langle \mathbf{u}_1,\mathbf{u}_1 \rangle + \lambda_1\lambda_1 = 1 \tag{46}$$

Order $p \geq 2$:

$$\mathbf{L}(\mathbf{V}_p) + 2\mathbf{Q}(\mathbf{V}_0, \mathbf{V}_p) = \lambda_p \mathbf{F} - \sum_{r=1}^{p-1} \mathbf{Q}(\mathbf{V}_r, \mathbf{V}_{p-r}) \qquad \langle \mathbf{u}_p, \mathbf{u}_1 \rangle + \lambda_p \lambda_1 = 0 \tag{47}$$

Details of the above expressions for the successive linear problems related to the order "p" are given in Appendix B as well as the finite element discretization of the set of linear equations to be solved for each ANM step. The key elements of the computational algorithm are summarized in Algorithm 4.

3.4.2. Validity domain

Since the solution $\mathbf{V}$ from ANM is a power series, it is required to determine the domain inside which the truncated series is sufficiently accurate. Given a precision ε, the series of displacement can be considered as sufficiently accurate when the last term of the series is very small with respect to the first term of the series as follows:

$$\frac{a^p \|\mathbf{u}_p\|}{\| \sum_{r=1}^{p} a^r \mathbf{u}_p \|} \approx \frac{a^p \|\mathbf{u}_p\|}{a \|\mathbf{u}_1\|} \leq \varepsilon \quad \Rightarrow \quad a \leq a_{max} = \left(\varepsilon \frac{\|\mathbf{u}_1\|}{\|\mathbf{u}_p\|} \right)^{\frac{1}{p-1}} \tag{48}$$

3.4.3. Forward progress of equilibrium path

Similarly to the Riks method, in Eq.(46), there are two solutions of λ_1 and we need to choose the one which guarantees the forward progress in the equilibrium path. It can be guaranteed by the criterion below (Zahrouni et al. (1999)):

$$\langle \frac{\partial \mathbf{u}_0}{\partial a}, \mathbf{u}_1 \rangle > 0 \tag{49}$$

4. Numerical examples

4.1. Lateral buckling of a cantilever beam

This example considers the lateral buckling of a cantilever beam described in Figure 5. The beam, with a length equal to 100m, is clamped at its left end and loaded at its right end by a vertical load F_Z, perturbed by a slight lateral load $F_X = 0.01\ F_Z$. The cross-section of the beam is rectangular with a height of 10m and a width of 1m. Young's modulus E of is equal to 100GPa and Poisson's ratio ν is equal to 0.3. The beam is discretized by 2×10 8-node quadrilateral 7-parameter shell elements with $2 \times 2 \times 2$ Gauss integration points. The objective of this example is to compare the performance of the improved EAS Newton-Raphson (improved NR) procedure with the classical Newton-Raphson (NR) procedure.

The convergence criterion ε_{NR} is based on the relative error of the residual vector:

$$\varepsilon_{NR} = \frac{\| \mathbf{R} \|}{\| \mathbf{f}_{int} \|} \leq 10^{-3} \tag{50}$$

where $\mathbf{R}$ denotes the residual vector and $\mathbf{f}_{int}$ denotes the vector of internal force. The load increment $\Delta\lambda = 0.02$ is fixed. In the classical NR procedure, the residual vector includes both the equilibrium residual and the EAS residual coming from the orthogonality condition, whereas the improved NR

Algorithm 4 ANM procedure

Require: $\mathbf{q}_0, \lambda_0$

Set $(\mathbf{q}^{(0)}, \alpha^{(0)}) = (\mathbf{q}_0, \alpha_0)$ and evaluate $[\mathbf{K}_T] = [\mathbf{K}_T(\mathbf{q}^{(0)})]$ and $\mathbf{f}_{int} = \mathbf{f}_{int}(\mathbf{q}^{(0)}, \alpha^{(0)})$

Set $k = 1$

while $k \leq N_{max}$ **do**

if $k = 1$ **then**

Evaluate $\hat{\mathbf{q}}_1 = [\mathbf{K}_T(\mathbf{q}_0)]^{-1}\mathbf{F}$, $\lambda_1 = \dfrac{\pm 1}{\sqrt{\langle \hat{\mathbf{q}}_1, \hat{\mathbf{q}}_1 \rangle + 1}}$ and $\mathbf{q}_1 = \lambda_1 \hat{\mathbf{q}}_1$

Evaluate $\hat{\mathbf{S}}_1 = [\mathbf{D}][\tilde{\mathbf{B}}(\mathbf{q}_0)]\mathbf{q}_1$

else

Evaluate $\mathbf{S}_p^{nl} = [\mathbf{D}] \sum_{r=1}^{p-1} \frac{1}{2}[\mathbf{B}^{nl}(\mathbf{q}_r)]\mathbf{q}_{p-r}$ and $\mathbf{R}_{\alpha,p} = -\sum_{r=1}^{p-1} \int_\Omega [\mathbf{B}_\alpha]^T \mathbf{S}_p^{nl} \, d\Omega$

Evaluate $\mathbf{F}_p^{nl} = -\sum_{r=1}^{p-1} \int_\Omega [\mathbf{B}^{nl}(\mathbf{q}_r)]^T \mathbf{S}_{p-r} \, d\Omega - \int_\Omega [\bar{\mathbf{B}}(\mathbf{q}_0)]^T \mathbf{S}_p^{nl} \, d\Omega$

Evaluate $\mathbf{q}_p^{nl} = [\mathbf{K}_T(\mathbf{q}_0)]^{-1} \bigwedge_{n=1}^{N_e} (\mathbf{F}_p^{nl} - [\mathbf{K}_{\alpha u}]^T [\mathbf{K}_{\alpha\alpha}]^{-1} \mathbf{R}_{\alpha,p})$

Evaluate $\mathbf{q}_p = \dfrac{\lambda_p}{\lambda_1}\mathbf{q}_1 + \mathbf{q}_p^{nl}$ and $\alpha_p = [\mathbf{K}_{\alpha\alpha}]^{-1}(\mathbf{R}_{\alpha,p} - [\mathbf{K}_{\alpha u}]\mathbf{q}_p)$

Evaluate $\mathbf{S}_p = [\mathbf{D}]\{[\bar{\mathbf{B}}(\mathbf{q}_0)]\mathbf{q}_p + [\mathbf{B}_\alpha]\alpha_p\} + \mathbf{S}_p^{nl}$

end if

end while

Evaluate $a_{max} = \left(\varepsilon \dfrac{\|\mathbf{q}_1\|}{\|\mathbf{q}_p\|} \right)^{\frac{1}{p-1}}$, $\Delta\mathbf{q} = \sum_{p=1}^{N_{max}} a_{max}^p \mathbf{q}_p$ and $\Delta\lambda = \sum_{p=1}^{N_{max}} a_{max}^p \lambda_p$

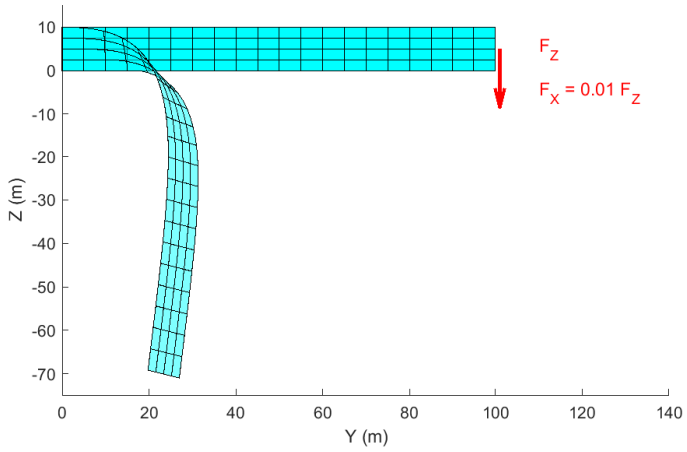

Figure 5: FE model of the cantilever beam in its undeformed configuration along with its final configuration after buckling

procedure only requires to check the equilibrium residual.

The lateral and vertical displacements of the loaded node obtained from the two computations are plotted in Figure 6 as a function of the load factor. It can be seen that both equilibrium paths exactly match. To assess the performance of the two NR procedures, the relative errors and the numbers of NR iterations required for each load increment are presented in Figure 7. It can be noted first that, when the number of iterations is the same in both procedures, the relative error of the improved NR is less than the classical one. Second, the number of iterations is slightly reduced for the improved NR procedure. It is worth noting that, in addition to provide a better accuracy and to reduce the number of iterations, the improved procedure has a strong advantage with respect to the classical procedure in terms of data memory management because it does not need anymore to conserve the EAS parameters α at every Gauss point. In the following numerical examples, we adopt the improved NR procedure.

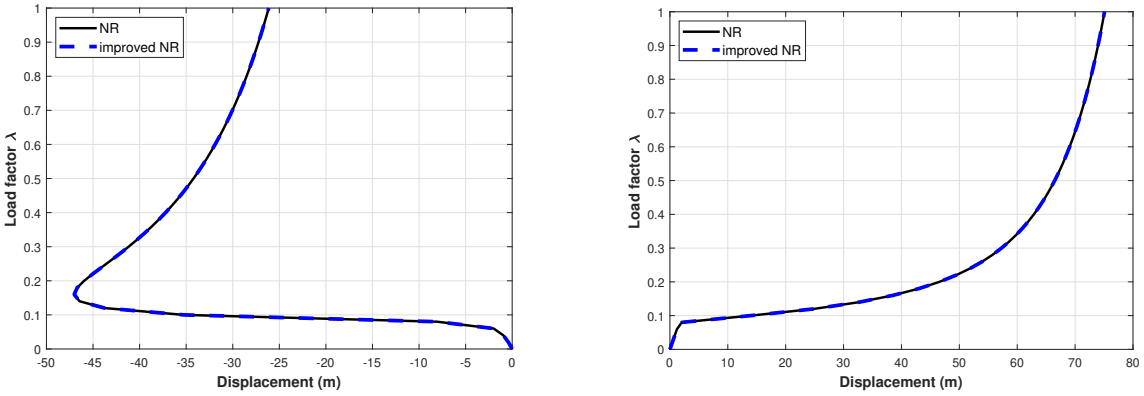

(a) Lateral displacement

(b) Vertical displacement

Figure 6: Lateral and vertical displacements of the loaded node versus the load factor λ: Newton-Raphson (NR) procedure and improved Newton-Raphson (Improved NR) procedure

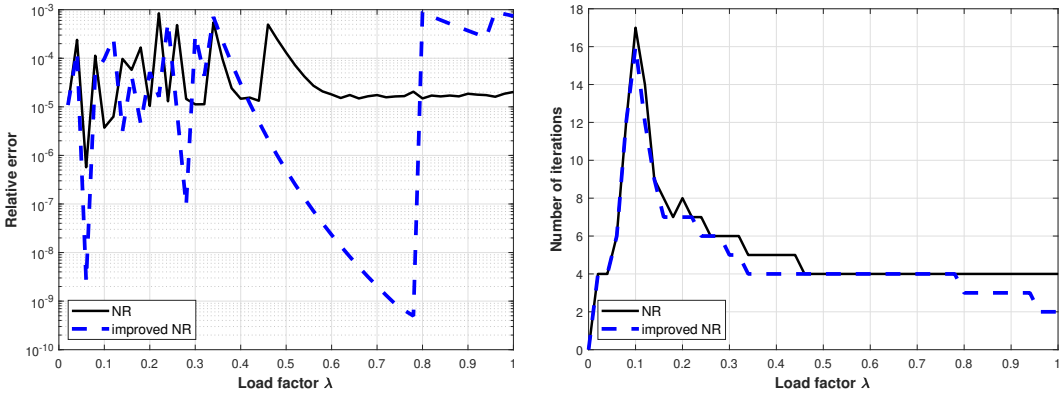

Figure 7: Relative errors and number of iterations versus the load factor λ: Newton-Raphson (NR) procedure and improved Newton-Raphson (Improved NR) procedure

4.2. Snap-through of a cylindrical shell

The classical test of cylindrical shell buckling is studied in this section to illustrate the performance of different methods in solving the non-linear problem with the presence of snap-through phenomena. The geometric and material parameters are chosen from Kuhl and Ramm (1999), as presented in Figure 8. The shell has a thickness of $t = 0.1$m, a total length of $L = 5$m, a radius of curvature of $R = 5$m, and a total angle of curvature of $\theta = \pi/3$. The elastic material is characterized by Lamé coefficients $\lambda = \mu = 8.10^{10}$ N/m^2. Only one quarter of the structure is modeled by considering the symmetry conditions as shown in Figure 8. The structure is discretized by 4×4 8-node quadrilateral 7-parameter shell elements with $2 \times 2 \times 2$ Gauss integration points. The computations using Riks method with different arc-length parameters are compared with the ANM procedure. In addition, a computation using the Newton-Raphson method is added to highlight the ability of path-following procedures (Riks and ANM) to predict the complex equilibrium path. Thus, four computations are carried out:

- Newton-Raphson method - Load control - $\Delta\lambda = 0.02$ - $\varepsilon_{NR} = 10^{-6}$
- Riks method - $\varepsilon_{NR} = 10^{-6}$ - with value of arc-length $s = 0.05$
- ANM - Order $p = 10$ - $\varepsilon_{ANM} = 10^{-7}$
- Reference results: ANM - Order $p = 10$ with 20-node hexahedral elements - $\varepsilon_{ANM} = 10^{-7}$

In this test, for the computations using the Newton-Raphson (NR) method and Riks method, the convergence criterion ε_{NR} is again based on the relative error of the global residual vector, taken here as equal to 10^{-6}. For the NR computations, the increment $\Delta\lambda = 0.02$ is fixed. For the Riks computation, the optimized value of the arc-length parameter s equal to 0.05 is adopted to obtain a forward and complete equilibrium path. For the ANM computations, the order of the series for the solution is fixed at $p = 10$, and the precision for evaluating the validity domain is $\varepsilon_{ANM} = 10^{-7}$.

The vertical displacements of points M and B, located on the cylindrical shell, as displayed in Figure 8, are plotted in Figure 9, exhibiting a rather complex equilibrium path during the buckling stage.

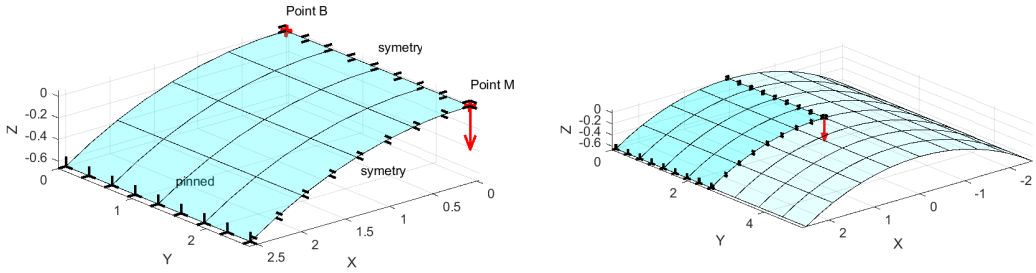

Figure 8: Model of cylindrical shell under vertical load

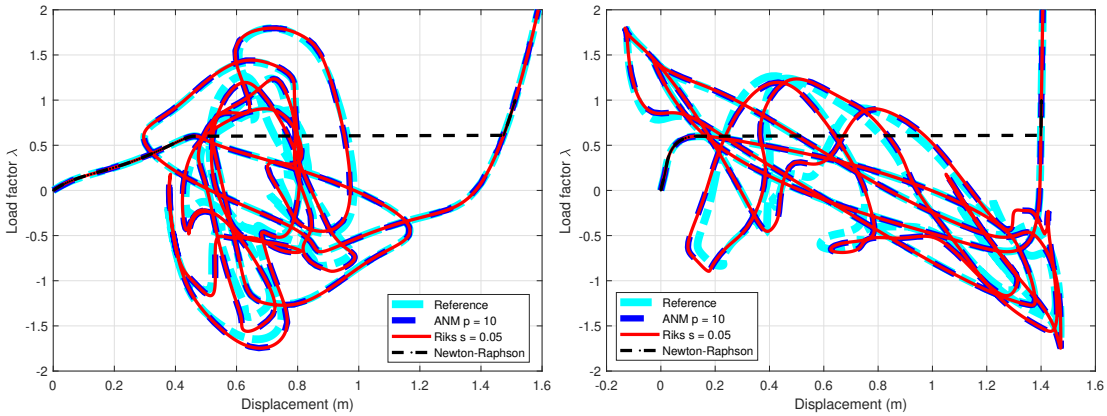

(a) Point M (b) Point B

Figure 9: Vertical displacements at point M (a) and point B (b) obtained by different methods: the ANM, the Riks method, and Newton-Raphson method. The reference is obtained from the computation with 3D model (20-node hexahedral element) using ANM.

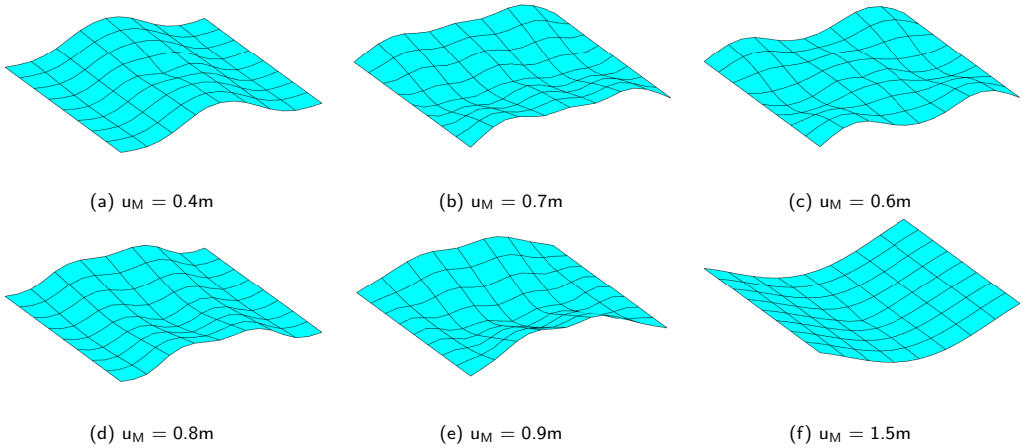

(a) $u_M = 0.4m$ (b) $u_M = 0.7m$ (c) $u_M = 0.6m$

(d) $u_M = 0.8m$ (e) $u_M = 0.9m$ (f) $u_M = 1.5m$

Figure 10: Different deformed configurations of the structure while load factor $\lambda = 1.0$

The snap-through phenomenon predicted by the Newton-Raphson computation is very consistent with the static solution based on load control given in Kuhl and Ramm (1999): the triggering point is

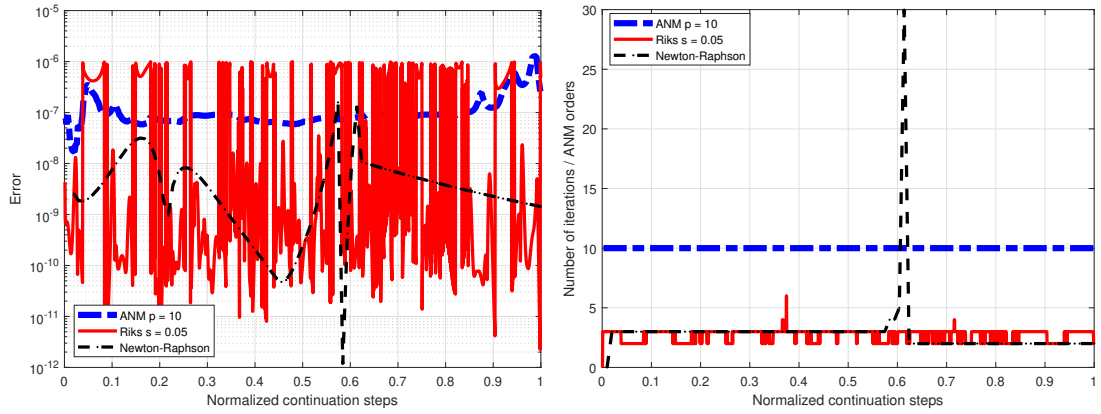

(a) Residual error

(b) Number of iterations

Figure 11: Relative residual error (a) and number of iterations (b) during the different computations: Riks method with $s = 0.05$, ANM with $p = 10$ and Newton-Raphson.

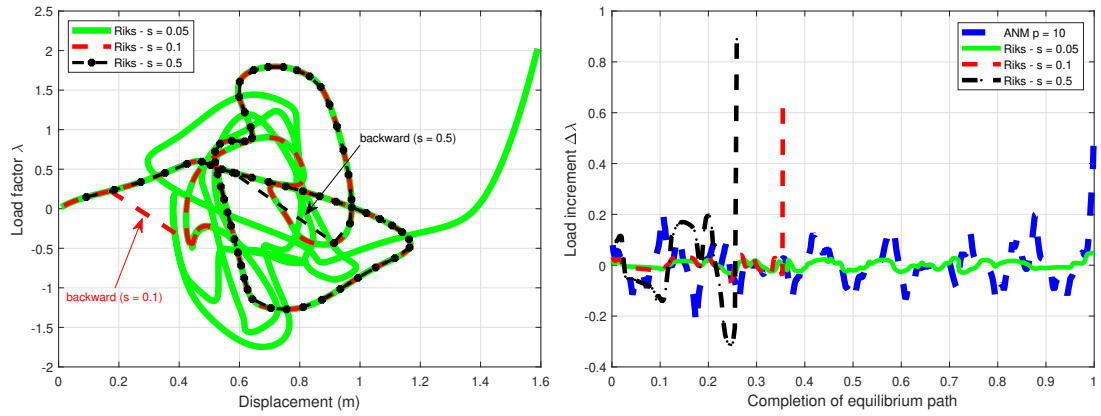

(a) Vertical displacement at point M

(b) Variation of load increment

Figure 12: Vertical displacement at point M (a) and the variation of the load increment (b) during the computations using the Riks method with different fixed arc-length conditions ($s = 0.5, 0.1, 0.05$)

	Riks method			ANM		
	$s = 0.50$	$s = 0.10$	$s = 0.05$	$p = 20$	$p = 10$	$p = 5$
Completion	0.25	0.35	1.00	1.00	1.00	1.00
N. of steps	28	334	1818	211	425	2504
N. of $\mathbf{K}_T$	133	1039	4919	211	425	2504
Normalized CPU	–	–	0.40	1.00	0.55	0.98

Table 1: Equilibrium path completion, number of continuation steps, number of evaluations of tangent operator and normalized computational time from different computations: Riks method (with $s = 0.50, 0.10, 0.05$) and ANM (with $p = 20, 10, 5$)

characterized by a displacement of point M equal to 0.43m and a load factor of 0.6, as well as a final displacement at the end of the snap-through equal to 1.5m. In the following, shell results are compared to the reference results provided by a 3D computation with hexahedral elements and ANM procedure.

As expected, it is observed that the solution obtained from the NR method presents a snap-through phenomenon and thus cannot predict such a complex buckling equilibrium path. Nonetheless, before and after the buckling stage, numerical results from the NR procedure match Riks and ANM procedures. The solutions obtained from the Riks method with the arc-length $s = 0.05$ and the ANM method closely match along the whole equilibrium path. Figure 10 displays different deformed configurations of the structure for the load factor $\lambda = 1.0$ in which very various deformed configurations can be seen up to the final configuration at displacement of point M equal to 1.5m on the ascending branch of the equilibrium path. In Figure 11, the relative errors of the residual vector and the number of iterations for all the considered computations, are plotted as a function of the normalized continuation path (from 0 to 1 to cover the whole equilibrium path). It can be observed that with a fixed load increment $\Delta\lambda = 0.02$, the NR procedure needs about 2 or 3 iterations to converge for each step. It is shown that, at the vicinity of the critical point, NR computation requires more iterations, up to 30 iterations. In comparison, it can be observed that the Riks method requires fewer iterations, varying from 2 or 3 iterations along the whole equilibrium path. Nonetheless, the prediction of the equilibrium path with the Riks method required a very low arc-length parameter s, equal to 0.05. The number of iterations of the ANM method is always the same, equal to 10 corresponding to the fixed order of the Taylor series to represent the displacements and loads.

The sensitivity of the results obtained with the Riks method as a function of the arc-length parameter is studied. The equilibrium path is again displayed in Figure 12a with fixed values of the arc-length parameter, equal to 0.05, 0.1, and 0.5. The smallest value achieves to predict the whole forward equilibrium path but not the two larger values for which backward paths are predicted. The failure of the Riks method is also displayed more clearly in Figure 12b in which the size of the load increment is plotted as a function of the completion of the equilibrium path (from 0 to 1 to cover the whole equilibrium path). It is shown that the Riks method fails at about 25% of the equilibrium path for $s = 0.5$ and at about 35% of the equilibrium path for $s = 0.1$. When adopted $s = 0.05$, the complete equilibrium path is predicted by the Riks method but it can be seen that the size of the load increment for the Riks method is lower than the size of the load increment allowed by the ANM method. The number of continuation steps, number of evaluations of the tangent operator $[\mathbf{K}_T]$ as well as the computational time of the Riks and ANM computations are summarized in Table 1. Two additional ANM computations with $p = 20$ and $p = 5$ are added to investigate the influence of the order of the truncated Taylor series. First, it has to be noted that all the ANM computations, with $p = 5, 10, 20$, achieve to predict the complete equilibrium path. In terms of computation time, the optimized order is $p = 10$. Indeed, considering lower value increases the number of ANM steps and increasing the order reduces the number of ANM steps but with more numerical effort for computing each ANM step. Comparing to the Riks method, the computation times related to the ANM procedure are higher. This is due to the reduced size of the discrete problem under investigation. Indeed, it is important to note that Riks method with $s = 0.05$ requires a number of buildings and factorizations of the tangent

operator ten times higher than ANM method with $p = 10$ which could have an important impact on the computation time as highlighted in the following discrete problems. Owing to the complexity of the predicted load-displacement curves for this buckling problem, the relevance of the 7-parameter shell element has to be highlighted as well as the effectiveness of the adopted solving procedures. In the following tests, the use of the 7-parameter shell element is investigated for thin-walled beams thanks to the proposed coupling approaches.

4.3. Buckling of steel cantilever L-shaped cross-section thin-walled beam

The buckling of the steel cantilever L-shaped cross-section beam is studied in this subsection. The geometry of the beam is presented in Figure 13. The beam is clamped at one end ($x = 0$) and loaded at another end ($x = 1.0$m) by a vertical load $F_Z = 100$kN, perturbed by a lateral load $F_Y = 0.1F_Z$. The L-shaped cross-section of the beam is characterized by: total height $h = 200$mm, flange's width $b = 200$mm, and flange's thickness $t_f = 5$mm. The steel material has Young's modulus E of 210GPa and Poisson's ratio ν of 0.24. In this test, the buckling of the structure is investigated by plotting the vertical displacements at the two points A, at the corner between the flanges, and B, at the end of the flange, as displayed in Figure 13 in which a refined mesh composed of 3D 20-node hexahedral elements is considered to provide the reference results.

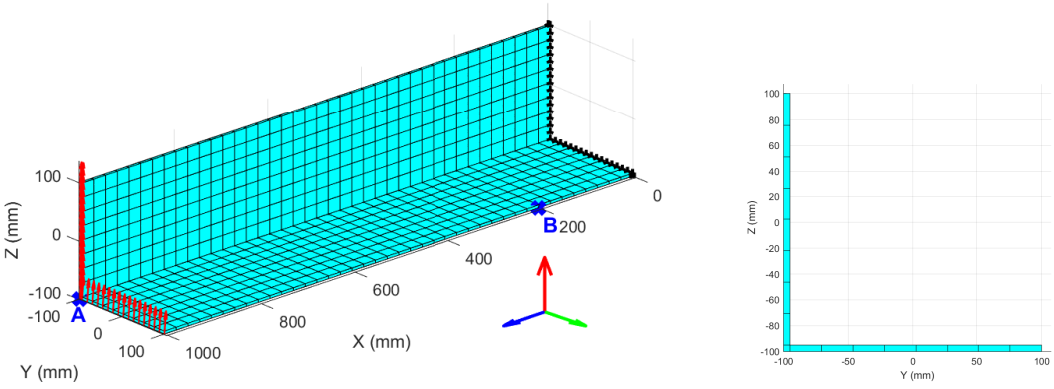

(a) Reference model (20-node hexahedral element)

(b) Cross-section of the beam

Figure 13: Description of the cantilever L-shaped cross-section beam with recording points A and B ; (a) reference model with 20-node hexahedral elements ; (b) cross-section of the beam

The structure is discretized in space by the 8-node 7-parameter shell elements (7-p shell) with $2 \times 2 \times 2$ integration points. The coupling between flanges is dealt with the two methods presented in Section 2.3: first, the dual method (DUAL) using improved-NR procedure and second the simplified method with the pre-processing procedure (PRE) to modify the shell directors at the nodes close to the corner.

To evaluate the mesh sensitivity for the two coupling strategies, three meshes as displayed in Figure (14): a fine mesh with the smaller interface elements (Mesh 1), a coarse mesh with smaller interface elements (Mesh 2), and the fine mesh with the same element size (Mesh 3). Figure 15 displays the

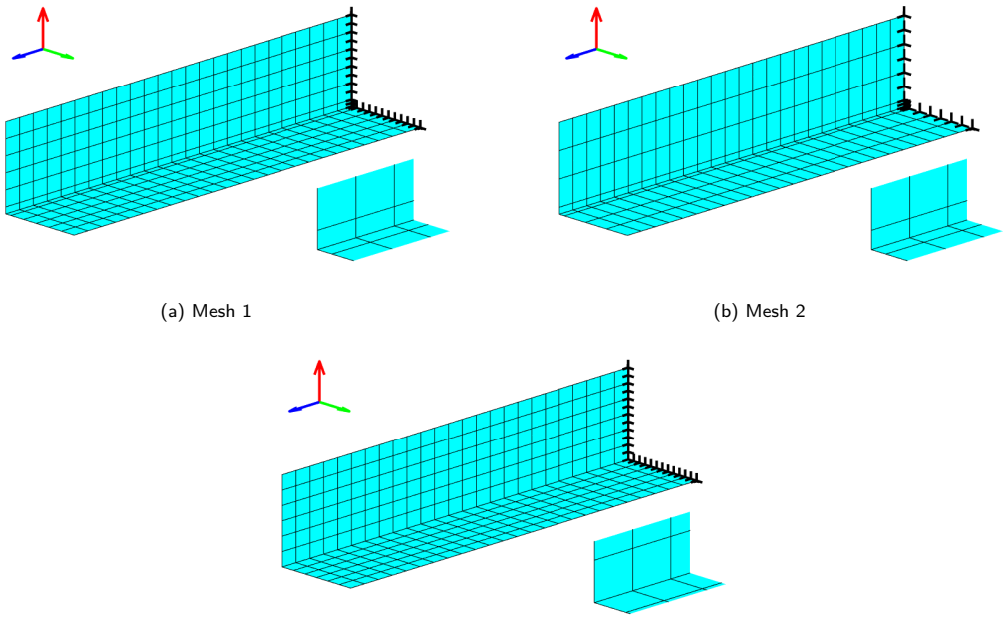

(a) Mesh 1

(b) Mesh 2

(c) Mesh 3

Figure 14: Three meshes composed of 7p-shell elements: a fine mesh with smaller interface elements (Mesh 1), a coarse mesh with smaller interface elements (Mesh 2) and a fine mesh with the same finite element size (Mesh 3)

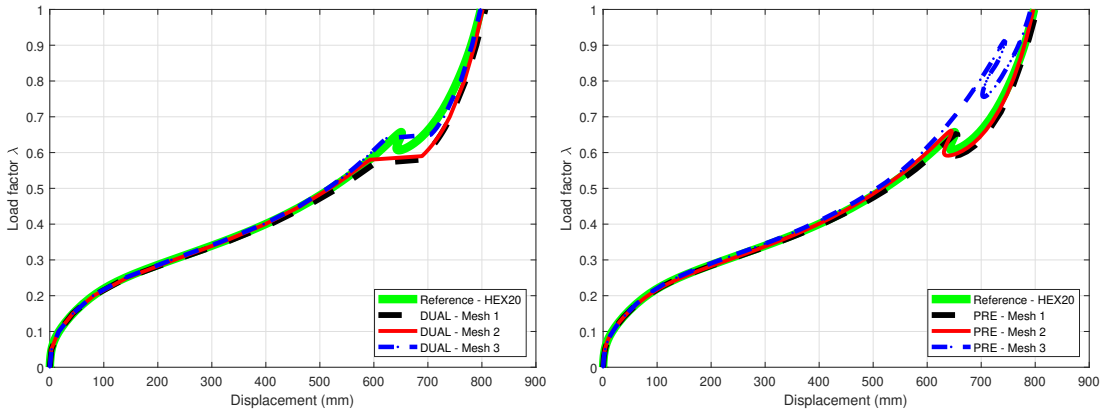

(a) Displacement at point A : DUAL method

(b) Displacement at point A : PRE method

Figure 15: Displacements at point A obtained for the three meshes using: (a) dual coupling strategy ; (b) the pre-processing strategy. Reference results are obtained with hexahedral elements and ANM procedure.

vertical displacements at point A obtained for the two coupling strategies (DUAL and PRE), with different meshes, compared to the reference results. It can be seen that the DUAL method achieves to predict in a satisfactory way the equilibrium path for the three meshes, whereas bigger discrepancies are highlighted for the PRE method for Mesh 3, that is without smaller elements at the interface. It is concluded that, when finer elements are set up at the interface between plates, both coupling strategies are able to predict the equilibrium path. Finally, in Figure 16, it is verified that the deformed configurations at the load factor $\lambda = 0.65$, from the reference 3D model and the shell model with Mesh

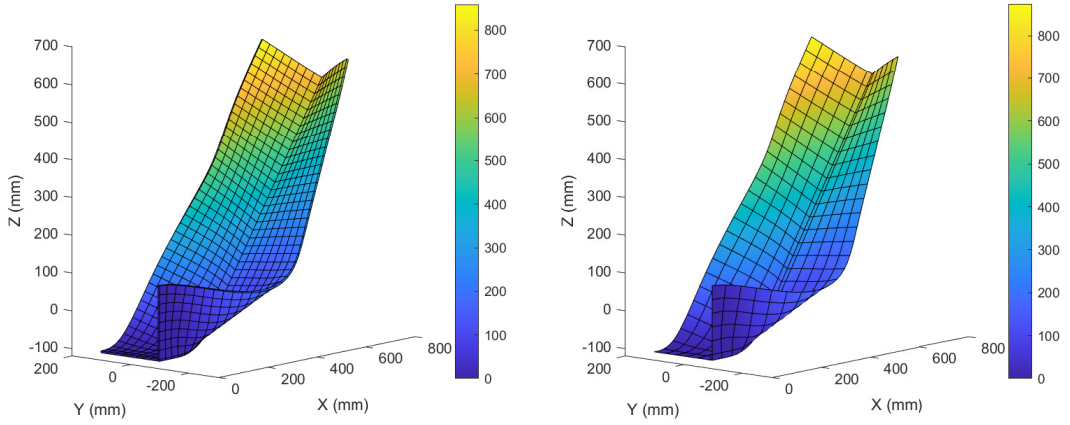

(a) Reference (20-node hexahedral model) - ANM (b) Mesh 1 - pre-processing coupling strategy - ANM

Figure 16: Deformed configurations of the L-shaped beam at critical points ($\lambda = 0.65$), along with the isovalues of displacement in mm, obtained from two models: reference model and the shell model of Mesh 1 using pre-processing coupling strategy.

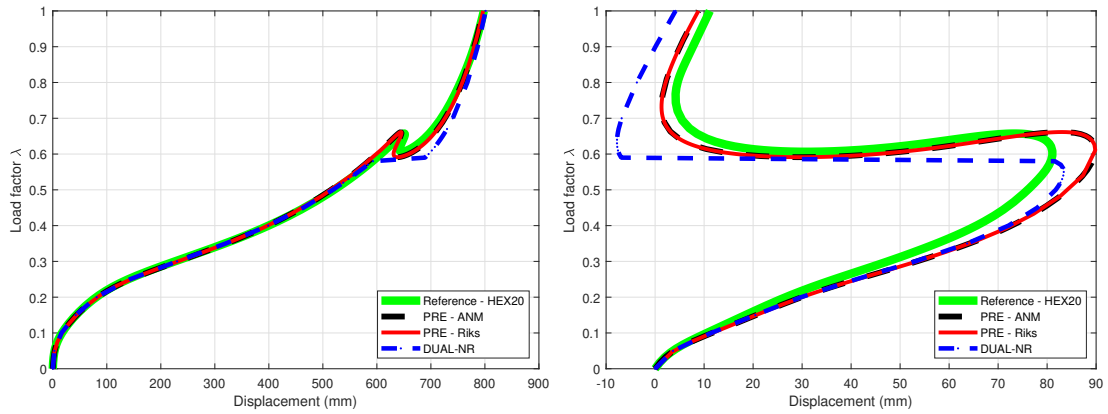

(a) Displacement at point A (b) Displacement at point B

Figure 17: Vertical displacement at point A (a) and at point B (b) obtained from the reference model and Mesh 2: the model using pre-processing coupling strategy is computed by the ANM (PRE-ANM) and the Riks method (PRE-Riks), and the model using the dual coupling strategy is computed by the Newton-Raphson method (DUAL-NR).

1, are very consistent between each other.

Then the Mesh 2 is adopted so as to compare the performance of the Riks method and ANM. Figure 17 displays the vertical displacement of points A and B obtained for Mesh 2 using the pre-processing coupling strategy with Riks and ANM solution procedures. It can be seen that both methods give consistent results with small discrepancies for the vertical displacement of point B. The residual errors of the computations are well controlled as seen in Figure 18. Table 2 compares the number of continuation steps, the number of evaluations of the tangent operator, and the computational time of the ANM and Riks computations. It can be seen that the Riks computation needs 1060 continuation steps to complete the equilibrium path, corresponding to 2985 evaluations of the tangent operator, whereas ANM with $p = 10$ only needs 47 continuation steps, corresponding to 47 evaluations of the

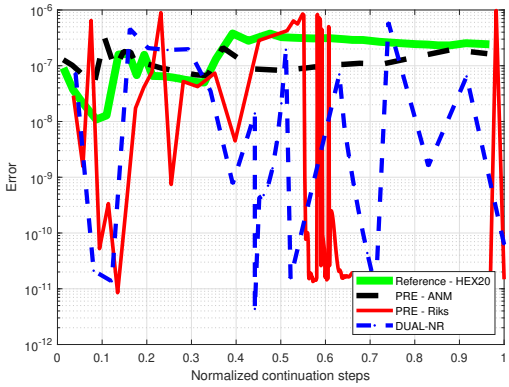

Figure 18: Relative error from the reference model and the models of Mesh 2: the model using pre-processing coupling strategy is computed by the ANM (PRE-ANM) and the Riks method (PRE-Riks), and the model using the dual coupling strategy is computed by the Newton-Raphson method (DUAL-NR).

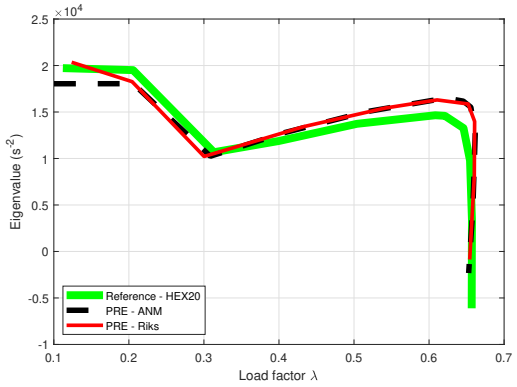

Figure 19: Evolution of the smallest eigenvalue ω^2 obtained from the reference model and models with Mesh 2 using pre-processing coupling strategy (PRE) computed using the ANM and Riks method.

tangent operator. Thus, in terms of computational time, ANM is here ten times more efficient than Riks method, contrarily to the previous case corresponding to a very small size discrete problem.

Following the lines of Boutyour et al. (2006), critical points on the equilibrium path can be determined by studying the eigenvalues of the system $\mathbf{M}^{-1}\,\mathbf{K}_{\text{tan}}$, where $\mathbf{M}$ is the mass matrix and $\mathbf{K}_{\text{tan}}$ is the tangent stiffness matrix given in Eq.(34). The evolution of the smallest eigenvalue ω^2 is plotted as a function of the load factor in Figure 19: the instability is detected when the eigenvalue ω^2 becomes negative. It can be observed that result from both computations (PRE with Riks and ANM) are very close to the reference results, giving critical loads at about $\lambda = 0.65$.

	ANM p = 10	Riks s = 0.05
N. of steps	47	1060
N. of $\mathbf{K}_T$	47	2985
Normalized CPU	0.09	1.00

Table 2: Number of continuation steps, number of evaluations of tangent operator and normalized computational time from the models of Mesh 2 (4000 degrees of freedom) using the ANM and the Riks method.

4.4. *Buckling of steel cantilever I-shaped cross-section thin-walled beam*

The global and local buckling of the steel cantilever I-shaped cross-section thin-walled beam is studied in this subsection. The geometry of the beam is presented in Figure 20. The beam is clamped at one end (x = 0) and loaded at another end (x = 1.5m) by a vertical load F_Z = –400kN, perturbed by a lateral load $F_Y = 0.1F_Z$. The I-shaped cross-section of the beam is characterized by: total height h = 200mm, flange's width b = 200mm, flange's and web's thickness $t_f = t_w$ = 5mm. The steel material has Young's modulus E of 210GPa and Poisson's ratio ν of 0.24. To follow the global buckling of the structure and local buckling of the bottom flange, the vertical displacement at the two points A located at the free end of the beam, and B located on the lower flange are considered, as displayed in Figure 20. Here, the refined mesh with 20-node hexahedral elements is considered for calculating the reference results.

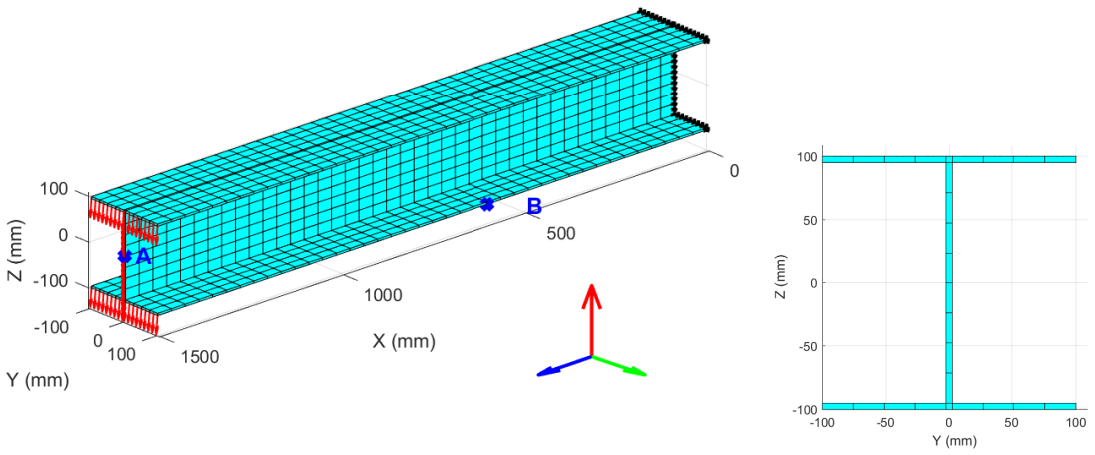

(a) Reference model (20-node hexahedral element)

(b) Cross-section of the beam

Figure 20: Description of the cantilever I-shaped cross-section beam with the recording points A and B ; (a) reference model discretized with 20-node hexahedral elements ; (b) cross-section of the beam.

The structure is discretized in space by the 8-node 7-parameter shell elements (7-p shell) with $2 \times 2 \times 2$ integration points. As previously done, three meshes displayed in Figure (21) are considered: a fine mesh with smaller interface elements (Mesh 1), a coarse mesh with smaller interface elements (Mesh 2) and the fine mesh with the same element size (Mesh 3).

Figure 22 displays the vertical displacement at point A obtained for the three meshes using the dual coupling strategy (DUAL) and the pre-processing procedure (PRE). It can be seen that the result from the pre-processing approach is less accurate with Mesh 3, that is when the same finite element size is adopted in the mesh. Indeed, the behaviour seems slightly stiffer in comparison to Meshes 1 and 2. It confirms that smaller interface elements are suitable for accurately predicting the equilibrium path. For the fine and coarse meshes with the presence of smaller interface elements between plates (Meshes 1 and 2), accurate results in comparison to the reference results are achieved.

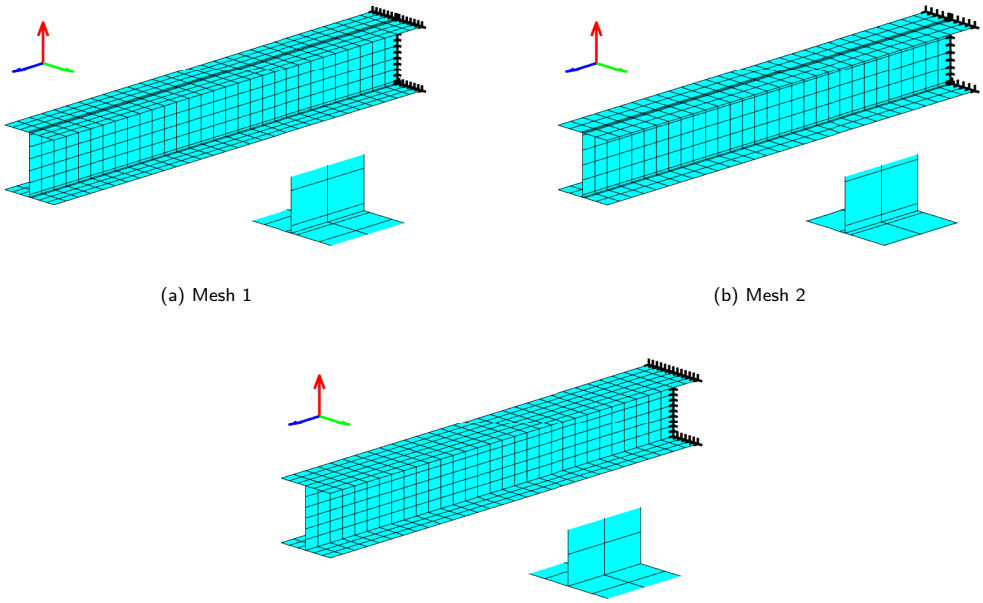

(a) Mesh 1

(b) Mesh 2

(c) Mesh 3

Figure 21: Three meshes with 7p-shell elements: a fine mesh with smaller interface elements (Mesh 1), a coarse mesh with smaller interface elements (Mesh 2), and a fine mesh with the same finite element size (Mesh 3)

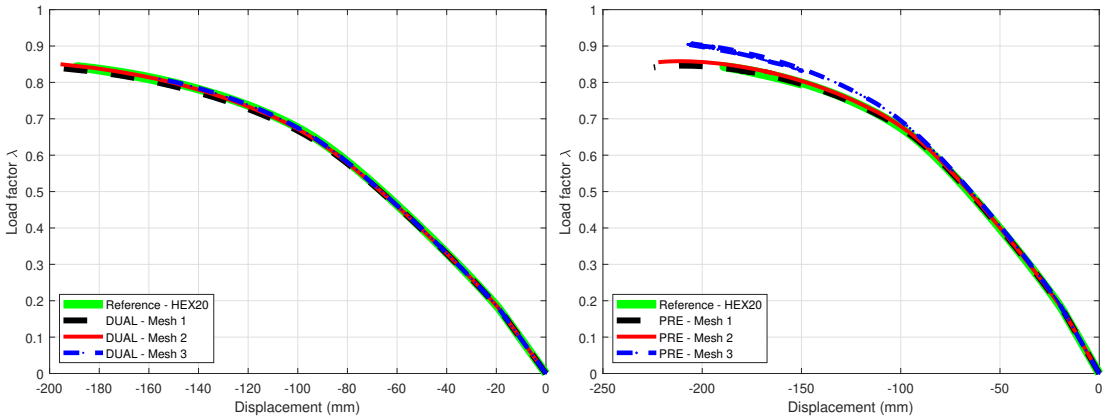

(a) Displacement at point A : DUAL method

(b) Displacement at point A : PRE method

Figure 22: Vertical displacements at point A obtained for the three meshes using (a) the dual coupling strategy with Newton-Raphson method (DUAL) and (b) the pre-processing strategy (PRE) with ANM compared to the reference results with ANM.

In the following, Mesh 2 is adopted. To illustrate the global buckling of the thin-walled beam, the vertical displacement at point A is plotted in Figure 23, along with a zoom on the critical points. All the computations are in a good agreement. In Figure 24, the eigenvalues are plotted. It can be seen that sightly different values of the loading parameter at the critical points are obtained: 0.83, 0.84 and 0.855 for the ANM computation with 7-p shells, the 3D reference computation and Riks computation with 7-p shells, respectively.

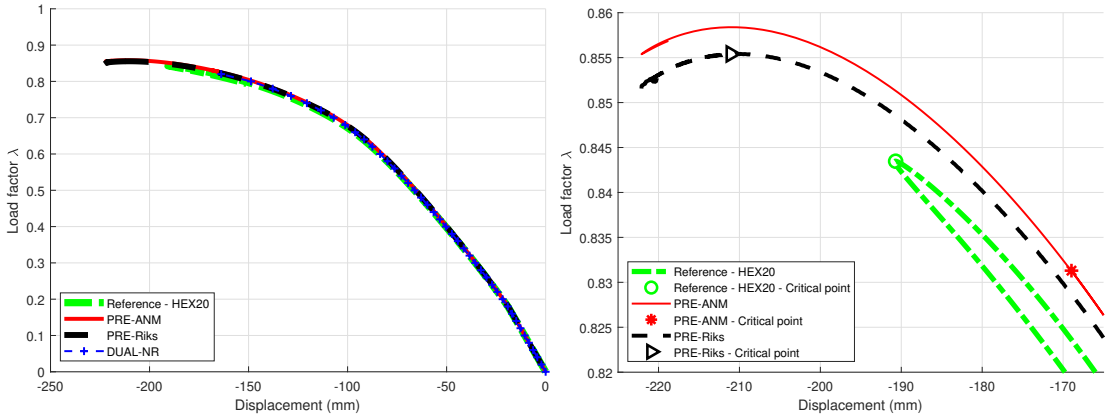

(a) Displacement at point A

(b) Displacement at point A (zoom on critical points)

Figure 23: Vertical displacement at point A (a) and zoom on the critical points (b) obtained from different computations: reference model with ANM (HEX20), 7-p shell model using ANM (PRE-ANM), 7-p shell model using Riks method (PRE-Riks), 7-p shell model using mortar coupling and Newton-Raphson method (DUAL-NR).

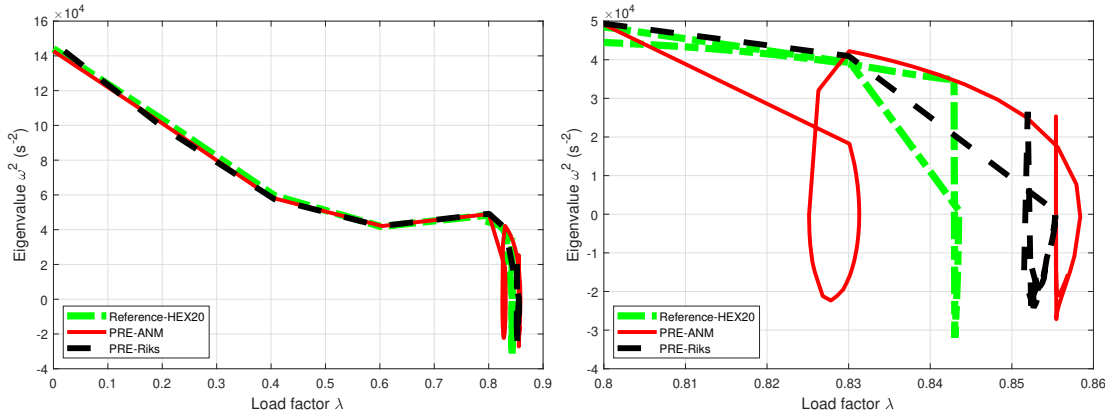

(a) Evolution of smallest eigenvalue

(b) Evolution of smallest eigenvalue (zoom on critical points)

Figure 24: Evolution of the smallest eigenvalue ω^2 (a) and zoom on the critical points (b) obtained with Mesh 2 using the pre-processing coupling strategy computed by the ANM and Riks method. The reference results are obtained from the 3D model computed by ANM.

The vertical displacement at point B, is plotted in Figure 25, so as to assess the sensitivity of the local buckling of the bottom flange. The first stage corresponding to the negative vertical displacement up to $\lambda = 0.60$ (in the direction of the vertical load), is well predicted by all the computations. Thus it can be concluded that both the dual coupling method and pre-processing method of the shell directors achieve to reproduce the equilibrium path before $\lambda = 0.60$. After this point, all the computations predict the change of the direction in vertical displacement, which becomes positive up to the critical points. Equilibrium paths at the critical stage, at about $\lambda = 0.82$, underlines the sensitivity of the local buckling of the bottom flange depending on the models (hexaedral or shells) as well as the solving procedure. In Figure 26, the relative residual error is plotted so as to verify the accuracy of the solution procedures, with an error less than the target criterion for convergence $\varepsilon_{NR} = 10^{-3}$. Finally, the deformed meshes are visualised in Figure 27 in the vicinity of the critical points for reference and 7-parameter shell models,

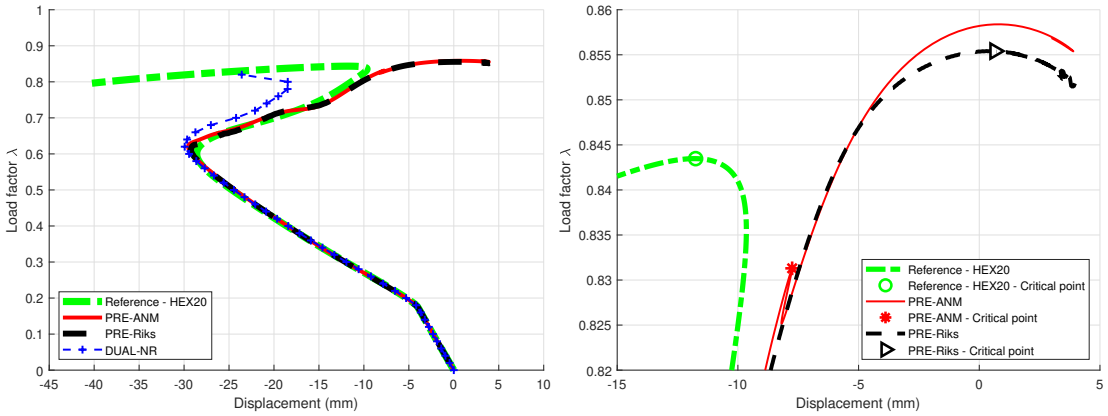

(a) Displacement at point B

(b) Displacement at point B (zoom on critical points)

Figure 25: Vertical displacement at point B (a) and zoom on the critical points (b) obtained with Mesh 2 using the pre-processing coupling strategy computed by the ANM and Riks method. The reference results obtained from the 3D model computed by the ANM.

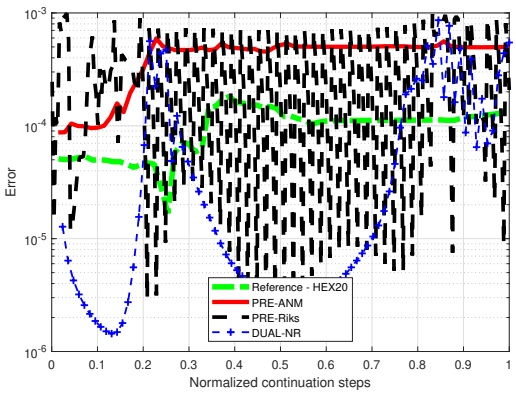

Figure 26: Residual error with Mesh 2 using the pre-processing coupling strategy computed by the ANM and the Riks method. The reference results obtained from the 3D model computed by the ANM.

exhibiting buckling waves at the bottom flange.

Table 3 compares the number of continuation steps, the number of evaluations of the tangent operator, and the computational time of the ANM and Riks procedures. It can be seen that the Riks computation needs 377 continuation steps to complete the equilibrium path, corresponding to 768 evaluations of the tangent operator, whereas ANM with p = 10 only needs 36 continuation steps, corresponding to 36 evaluations of the tangent operator. As a consequence, in terms of computation time, the ANM computation is here nine times faster than the Riks method.

5. Conclusion

Non-linear quasi-static buckling of thin-walled structures with arbitrary cross-sections has been analysed using efficient 7-parameter shell elements, endowed with the Enhanced Assumed strain concept enabling us to employ a three-dimensional law without any condensation technique. For this purpose, the mortar method has been set up, by considering the coupling on the two-dimensional interface

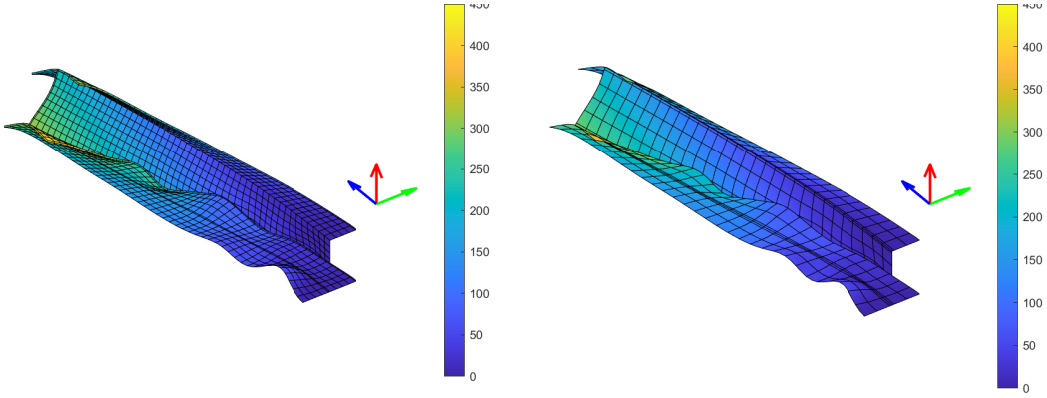

(a) Reference (20-node hexahedral element) (b) Mesh 2 - pre-processing coupling strategy

Figure 27: Bottom views (free condition on the left end of the beam and clamped condition on the right end) of the deformed configurations at the critical points obtained from different computations: reference model (a) at $\lambda = 0.84$, and the 7p- shell model (Mesh 2) with pre-processing coupling strategy at $\lambda = 0.86$.

	ANM p = 10	Riks s = 0.05
N. of steps	36	377
N. of $\mathbf{K}_T$	36	768
Normalized CPU	0.13	1.00

Table 3: Number of continuation steps, number of evaluations of the tangent operator, and normalized computational time from the models of Mesh 1 (10300 degrees of freedom) using the ANM and the Riks method.

between the plates. In addition, a simple pre-processing procedure has been explored, by simply prescribing simple rules for the determination of the shell directors at the nodes close to the interface. The accuracy and robustness of the two coupling approaches have been investigated by considering different meshes and three different solution strategies including Newton-Raphson, Newton-Riks and Asymptotic Numerical methods (ANM). Both coupling strategies achieve to predict the equilibrium path for L-shaped and I-shaped cross-section thin-walled beams in comparison to the reference results provided by three-dimensional analyses with 20-node hexahedral elements. ANM procedure with the pre-processing approach of the nodal shell directors beams turns out to be very efficient in terms of accuracy and robustness. Work is in progress to extend the ANM approach for thin-walled beams with arbitrary cross-sections and shell structures with stiffeners to the dynamic case, by comparing the ANM approach to classical transient strategies such as implicit and explicit time integration, as well as hybrid explicit/implicit multi time step approach.

Appendix A. Matrices for the finite element discretization of the 7-parameter shell element

$$[\mathbf{N}] = \begin{bmatrix} N^k & 0 & 0 & \theta^3 N^k & 0 & 0 & \\ 0 & N^k & 0 & 0 & \theta^3 N^k & 0 & \cdots k = 1,8 \\ 0 & 0 & N^k & 0 & 0 & \theta^3 N^k & \end{bmatrix} \tag{A.1}$$

$$[\mathbf{G}] = \begin{bmatrix} N^k_{,1} & 0 & 0 & \theta^3 N^k_{,1} & 0 & 0 & \\ 0 & N^k_{,1} & 0 & 0 & \theta^3 N^k_{,1} & 0 & \\ 0 & 0 & N^k_{,1} & 0 & 0 & \theta^3 N^k_{,1} & \\ N^k_{,2} & 0 & 0 & \theta^3 N^k_{,2} & 0 & 0 & \\ 0 & N^k_{,2} & 0 & 0 & \theta^3 N^k_{,2} & 0 & \cdots k = 1,8 \\ 0 & 0 & N^k_{,2} & 0 & 0 & \theta^3 N^k_{,2} & \\ 0 & 0 & 0 & N^k & 0 & 0 & \\ 0 & 0 & 0 & 0 & N^k & 0 & \\ 0 & 0 & 0 & 0 & 0 & N^k & \end{bmatrix} \tag{A.2}$$

$$[\mathbf{R}] = \begin{bmatrix} g_1^x & g_1^y & g_1^z & 0 & 0 & 0 & 0 & 0 & 0 \\ 0 & 0 & 0 & g_2^x & g_2^y & g_2^z & 0 & 0 & 0 \\ 0 & 0 & 0 & 0 & 0 & 0 & g_3^x & g_3^y & g_3^z \\ g_2^x & g_2^y & g_2^z & g_1^x & g_1^y & g_1^z & 0 & 0 & 0 \\ 0 & 0 & 0 & g_3^x & g_3^y & g_3^z & g_2^x & g_2^y & g_2^z \\ g_3^x & g_3^y & g_3^z & 0 & 0 & 0 & g_1^x & g_1^y & g_1^z \end{bmatrix} \tag{A.3}$$

$$[\mathbf{A}(\mathbf{q})] = \begin{bmatrix} s_1^x & s_1^y & s_1^z & 0 & 0 & 0 & 0 & 0 & 0 \\ 0 & 0 & 0 & s_2^x & s_2^y & s_2^z & 0 & 0 & 0 \\ 0 & 0 & 0 & 0 & 0 & 0 & s_3^x & s_3^y & s_3^z \\ s_2^x & s_2^y & s_2^z & s_1^x & s_1^y & s_1^z & 0 & 0 & 0 \\ 0 & 0 & 0 & s_3^x & s_3^y & s_3^z & s_2^x & s_2^y & s_2^z \\ s_3^x & s_3^y & s_3^z & 0 & 0 & 0 & s_1^x & s_1^y & s_1^z \end{bmatrix} \quad \text{where} \quad \hat{\mathbf{s}} = [\mathbf{G}]\mathbf{q} \tag{A.4}$$

$$[\mathbf{B}_\alpha] = \begin{bmatrix} 0 & 0 & 0 & 0 \\ 0 & 0 & 0 & 0 \\ \theta^3 & \theta^3\xi & \theta^3\eta & \theta^3\xi\eta \\ 0 & 0 & 0 & 0 \\ 0 & 0 & 0 & 0 \\ 0 & 0 & 0 & 0 \end{bmatrix} \tag{A.5}$$

$$[\mathbf{M}(\mathbf{S})] = \begin{bmatrix} S^{11} & 0 & 0 & S^{12} & 0 & 0 & S^{13} & 0 & 0 & \\ 0 & S^{11} & 0 & 0 & S^{12} & 0 & 0 & S^{13} & 0 & \\ & 0 & 0 & S^{11} & 0 & 0 & S^{12} & 0 & 0 & S^{13} \\ S^{12} & 0 & 0 & S^{22} & 0 & 0 & S^{23} & 0 & 0 & \\ 0 & S^{12} & 0 & 0 & S^{22} & 0 & 0 & S^{23} & 0 & \\ & 0 & 0 & S^{12} & 0 & 0 & S^{22} & 0 & 0 & S^{23} \\ S^{13} & 0 & 0 & S^{23} & 0 & 0 & S^{33} & 0 & 0 & \\ 0 & S^{13} & 0 & 0 & S^{23} & 0 & 0 & S^{33} & 0 & \\ & 0 & 0 & S^{13} & 0 & 0 & S^{23} & 0 & 0 & S^{33} \end{bmatrix} \tag{A.6}$$

Appendix B. Further details about Asymptotic Numerical Method

The expressions of $\mathbf{L}(.)$ and $\mathbf{Q}(.,.)$ and $\mathbf{F}$ are given below:

$$\mathbf{L}(\mathbf{V}) = \begin{cases} \displaystyle\int_\Omega \mathbf{E}^{l}(\delta\mathbf{u})^T : \mathbf{S}\, d\Omega \\ \mathbf{S} - \mathbf{D} : \left(\mathbf{E}^{l}(\mathbf{u}) + \tilde{\mathbf{E}}\right) \\ \displaystyle\int_\Omega \delta\tilde{\mathbf{E}} : \mathbf{S}(\mathbf{u}, \tilde{\mathbf{E}}) :\ d\Omega \end{cases}, \qquad \mathbf{F} = \begin{cases} P_e(\delta\mathbf{u}) \\ 0 \\ 0 \end{cases}$$

$$\mathbf{Q}(\mathbf{V}, \mathbf{V}) = \begin{cases} \displaystyle\int_\Omega 2\mathbf{E}^{nl}(\mathbf{u}, \delta\mathbf{u})^T : \mathbf{S}\, d\Omega \\ -\mathbf{D} : \mathbf{E}^{nl}(\mathbf{u}, \mathbf{u}) \\ 0 \end{cases} \tag{B.1}$$

By replacing in the above equation the mixed variable at order "p" $\mathbf{V}_p$ by $(\mathbf{u}_p, \mathbf{S}_p, \tilde{\mathbf{E}}_p)^T$, that is the displacement, the second Piola-Kirchhoff stress and the additional strain at order "p", we obtain for order $p \geq 2$:

$$\begin{aligned} &\cdot \int_\Omega [\mathbf{E}^{l}(\delta\mathbf{u}) + 2\mathbf{E}^{nl}(\mathbf{u}_0, \delta\mathbf{u})]^T : \mathbf{S}_p\, d\Omega + \int_\Omega +2\mathbf{E}^{nl}(\mathbf{u}_p, \delta\mathbf{u})^T : \mathbf{S}_0\, d\Omega = ... \\ &\qquad \lambda_p P_e(\delta\mathbf{u}) - \sum_{r=1}^{p-1} \int_\Omega 2\mathbf{E}^{nl}(\mathbf{u}_r, \delta\mathbf{u})^T : \mathbf{S}_{p-r}\, d\Omega \\ &\cdot \mathbf{S}_p = \mathbf{D} : \left(\mathbf{E}^{l}(\mathbf{u}_p) + 2\mathbf{E}^{nl}(\mathbf{u}_0, \mathbf{u}_p) + \tilde{\mathbf{E}}_p\right) + \sum_{r=1}^{p-1} \mathbf{D} : \mathbf{E}^{nl}(\mathbf{u}_r, \mathbf{u}_{p-r}) \\ &\cdot \int_\Omega \delta\tilde{\mathbf{E}}^T : \mathbf{S}_p = 0 \end{aligned} \tag{B.2}$$

From the system above, by substituting $\mathbf{S}_p$ from the second equation into the first and the third equations, we obtain the system of equations below:

$$
\begin{aligned}
&\cdot \int_\Omega [\mathbf{E}^l(\delta\mathbf{u}) + 2\mathbf{E}^{nl}(\mathbf{u}_0, \delta\mathbf{u})]^T : \mathbf{D} : [\mathbf{E}^l(\mathbf{u}_p) + 2\mathbf{E}^{nl}(\mathbf{u}_0, \mathbf{u}_p) + \tilde{\mathbf{E}}_p]\, d\Omega - \ldots \\
&\int_\Omega 2\mathbf{E}^{nl}(\mathbf{u}_p, \delta\mathbf{u})]^T : \mathbf{S}_0\, d\Omega = \lambda_p P_e(\delta\mathbf{u}) - \sum_{r=1}^{p-1} \int_\Omega 2\mathbf{E}^{nl}(\mathbf{u}_r, \delta\mathbf{u})^T : \mathbf{S}_{p-r}\, d\Omega \\
&- \sum_{r=1}^{p-1} \int_\Omega [\mathbf{E}^l(\delta\mathbf{u}) + 2\mathbf{E}^{nl}(\mathbf{u}_0, \delta\mathbf{u})]^T : \mathbf{D} : \mathbf{E}^{nl}(\mathbf{u}_r, \mathbf{u}_{p-r})\, d\Omega \\
&\cdot \int_\Omega \delta\tilde{\mathbf{E}}^T : \mathbf{D} : [\mathbf{E}^l(\mathbf{u}_p) + 2\mathbf{E}^{nl}(\mathbf{u}_0, \mathbf{u}_p) + \tilde{\mathbf{E}}_p]\, d\Omega = -\sum_{r=1}^{p-1} \int_\Omega \delta\tilde{\mathbf{E}}^T : \mathbf{D} : \mathbf{E}^{nl}(\mathbf{u}_r, \mathbf{u}_{p-r})\, d\Omega
\end{aligned}
\tag{B.3}
$$

The discretization by FEM is done as presented in the section devoted to the classical Newton-Raphson method. The second Piola-Kirchhoff stress at order "p" can be written as:

$$
\begin{aligned}
\mathbf{S}_p &= [\mathbf{D}]\{[\bar{\mathbf{B}}(\mathbf{q}_0)]\mathbf{q}_p + [\mathbf{B}_\alpha]\alpha_p\} + \mathbf{S}_p^{nl} \\
\mathbf{S}_p^{nl} &= [\mathbf{D}] \sum_{r=1}^{p-1} \frac{1}{2} [\mathbf{B}^{nl}(\mathbf{q}_r)]\mathbf{q}_{p-r}
\end{aligned}
\tag{B.4}
$$

The orthogonality condition can be written in matrix form as follows:

$$
\begin{aligned}
&\int_\Omega [\mathbf{B}_\alpha]^T [\mathbf{D}]([\bar{\mathbf{B}}(\mathbf{q}_0)]\mathbf{q}_p + [\mathbf{B}_\alpha]\alpha_p)\, d\Omega = -\sum_{r=1}^{p-1} \int_\Omega [\mathbf{B}_\alpha]^T \mathbf{S}_p^{nl}\, d\Omega = \mathbf{R}_{\alpha,p} \\
&\Rightarrow \alpha_p = [\mathbf{K}_{\alpha\alpha}]^{-1}(\mathbf{R}_{\alpha,p} - [\mathbf{K}_{\alpha u}]\mathbf{q}_p)
\end{aligned}
\tag{B.5}
$$

The equilibrium equation becomes (Zahrouni et al. (1999)):

$$
\begin{aligned}
&[\mathbf{K}_T(\mathbf{q}_0)]\mathbf{q}_p + [\mathbf{K}_{\alpha u}]^T \alpha_p = \lambda_p \mathbf{P} + \mathbf{F}_p^{nl} \\
&\mathbf{F}_p^{nl} = -\sum_{r=1}^{p-1} \int_\Omega [\mathbf{B}^{nl}(\mathbf{q}_r)]^T \mathbf{S}_{p-r}\, d\Omega - \int_\Omega [\bar{\mathbf{B}}(\mathbf{q}_0)]^T \mathbf{S}_p^{nl}\, d\Omega \\
&\Rightarrow [\mathbf{K}_T(\mathbf{q}_0)]\mathbf{q}_p = \lambda_p \mathbf{P} + \bigwedge_{n=1}^{N_e} (\mathbf{F}_p^{nl} - [\mathbf{K}_{\alpha u}]^T [\mathbf{K}_{\alpha\alpha}]^{-1} \mathbf{R}_{\alpha,p})
\end{aligned}
\tag{B.6}
$$

References

ABAQUS. *(2014) Theory Manual, Version 6.14*. Dassaults Systemes Simulia, Inc, 2014.

B. Asgarian, M. Soltani, and F. Mohri. Lateral-torsional buckling of tapered thin-walled beams with arbitrary cross-sections. *Thin-Walled Structures*, 62:96–108, 2013.

L. Azrar, B. Cochelin, N. Damil, , and M. Potier-Ferry. An asymptotic-numerical method to compute the post-buckling behaviour of elastic plates and shells. *International Journal for Numerical Methods in Engineering*, 36:1251–1277, 1993.

S. Baguet. *PhD Thesis: Stabilité des structures minces et sensibilité aux imperfections par la Méthode Asymptotique Numérique*. 2011.

S. Baguet and B. Cochelin. On the behaviour of the ANM continuation in the presence of bifurcation. *Communication in Numerical Methods in Engineering*, 19:459–471, 2003.

C. Bernardi, N. Debit, and Y. Maday. Coupling finite element with spectral methods: first results. *Mathematics of computation*, pages 21–39, 1990.

C. Bernardi, Y. Maday, and A. Patera. A new noncorforming approach to domain decomposition: The mortar element method. *Nonlinear partial differential equations and their applications: Collège de France Seminar*, 299:13–51, 1994.

M. Bischoff and E. Ramm. Shear deformable shell elements for large strains and rotations. *International Journal for Numerical Methods in Engineering*, 40:4427–4449, 1997.

M. Bischoff and E. Ramm. On the physical significance of higher order kinematic and static variables in a three-dimensional shell formulation. *International Journal of Solids and Structures*, 37:6933–6960, 2000.

E. Boutyour, H. Zahrouni, M. Potier-Ferry, and M. Boudi. Bifurcation points and bifurcation branches by asymptotic-numerical method and Padé approximants. *International Journal for Numerical Methods in Engineering*, 60:1987–2012, 2004.

E. Boutyour, L. Azrar, and M. Potier-Ferry. Vibration of buckled elastic structures with large rotations by an asymptotic numerical method. *Computers and Structures*, 84:93–101, 2006.

E. Brivadis, A. Buffa, B. Wohlmuth, and L. Wunderlich. Isogeometric mortar methods. *Computer Methods in Applied Mechanics and Engineering*, 284:292–319, 2015.

M. Brun, F. D. Martin, and N. Richart. Asynchronous SEM/FEM co-simulation for seismic analysis of concrete gravity dams. *Computers and Structures*, 245:106459, 2021.

N. Bütcher, E. Ramm, and D. Roehl. Three-dimensional extension of non-linear shell formulation based on the enhanced assumed strain concept. *International Journal for Numerical Methods in Engineering*, 37:2551–2568, 1994.

A.-K. Chau, M. Brun, and T. Elguedj. Hybrid Asynchronous Isogeometric Perfectly Matched Layer for transient elastodynamics. *Computers and Geotechnics*, 158:105387, 2023.

B. Cochelin. A path-following technique via an asymptotic-numerical method. *Computers and Structures*, 53:1181–1192, 1994.

B. Cochelin, N. Damil, and M. Poiter-Ferry. The asymptotic-numerical method: an efficient perturbation technique for non-linear structural mechanics. *Revue Européenne des Eléments Finis*, 3(2):281–297, 1994a.

B. Cochelin, N. Damil, and M. Potier-Ferry. Asymptotic-numerical method and Padé approximants for non-linear elastic structures. *International Journal for Numerical Methods in Engineering*, 37: 1187–1213, 1994b.

B. Cochelin, N. Damil, and M. Potier-Ferry. *Méthode asymptotique numérique*. Hermès-Lavoisier, Paris, 2007.

W. Dornisch, G. Vitucci, and S. Klinkel. The weak substitution method - an application of the mortar method for patch coupling in NURBS-based isogeometric analysis. *International Journal for Numerical Methods in Engineering*, 103:205–234, 2015.

A. Herrema, E. Johnson, D. Proserpio, M. Wu, J. Kiendl, and M.-C. Hsu. Penalty coupling of non-matching isogeometric Kirchhoff–Love shell patches with application to composite wind turbine blades. *Computer Methods in Applied Mechanics and Engineering*, 346:810–840, 2019.

M. Jamal, B. Braikat, S. Boutmir, N. Damil, and M. Potier-Ferry. A high order implicit algorithm for solving nonlinear problems. *Computational Mechanics*, 28:375–390, 2002.

D. Kuhl and E. Ramm. Generalized Energy-Momentum Method for non-linear adaptive shell dynamics. *Computer Methods in Applied Mechanics and Engineering*, 178:343–366, 1999.

MATLAB. *version 9.13.0 (R2022b)*. The MathWorks Inc., Natick, Massachusetts, 2022.

A. Najah, B. Cochelin, N. Damil, and M. Potier-Ferry. A critical review of asymptotic numerical methods. *Archives of Computational Methods in Engineering*, 5:3–22, 1998.

D. Proserpio, M. Ambati, L. D. Lorenzis, and J. Kiendl. Phase-field simulation of ductile fracture in shell structures. *Computer Methods in Applied Mechanics and Engineering*, 385:114019, 2021.

E. Ramm and W. Wall. Shell structures - a sensitive interrelation between physics and numerics. *International Journal for Numerical Methods in Engineering*, 60:381 – 427, 2004.

D. Roehl and E. Ramm. Large elasto-plastic finite element analysis of solids and shells with the enhanced assumed strain concept. *International Journal of Solids and Structures*, 33:3215–3237, 1996.

J. Simo and M. Rifai. A class of mixed assumed strain methods and the method of incompatible modes. *International Journal for Numerical Methods in Engineering*, 29:1595–1638, 1990.

M. Soltani and F. Mohri. Stability and vibration analyses of tapered columns resting on one or two-parameter elastic foundations. *Journal of Numerical Methods in Civil Engineering*, 15:57–66, 2016.

M. Soltani, B. Asgarian, and F. Mohri. Finite element method for stability and free vibration analyses of non-prismatic thin-walled beams. *Thin-Walled Structures*, 38:245–261, 2014.

P. Ventura, M. Potier-Ferry, and H. Zahrouni. A secure version of asymptotic numerical method via convergence acceleration. *Comptes Rendus Mécanique*, 348:361–374, 2020.

P. Ventura, H. Azzayani, H. Zahrouni, and M. Potier-Ferry. Buckling of pressurized cylindrical shells using the Asymptotic Numerical Method. *Thin-Walled Structures*, 188:110835, 2023.

H. Zahrouni, B. Cochelin, and M. Poiter-Ferry. Computing finite rotations of shells by an asymptotic-numerical method. *Computer Methods in Applied Mechanics and Engineering*, 175:71–85, 1999.

+